

High order numerical discretizations of the Einstein-Euler equations in the Generalized Harmonic formulation

Stefano Muzzolon^{a,c}, Michael Dumbser^b, Olindo Zanotti^{b,*}, Elena Gaburro^a

^a*Department of Computer Science, University of Verona, Strada le Grazie 15, Verona, 37134, Italy*

^b*Laboratory of Applied Mathematics, DICAM, University of Trento, via Mesiano 77, 38123 Trento, Italy*

^c*Department of Mathematics, University of Trento, Via Sommarive 14, 38123 Trento, Italy*

Abstract

We propose two new alternative numerical schemes to solve the coupled Einstein-Euler equations in the Generalized Harmonic formulation. The first one is a finite difference (FD) Central Weighted Essentially Non-Oscillatory (CWENO) scheme on a traditional Cartesian mesh, while the second one is an ADER (Arbitrary high order Derivatives) discontinuous Galerkin (DG) scheme on 2D unstructured polygonal meshes. The latter, in particular, represents a preliminary step in view of a full 3D numerical relativity calculation on moving meshes. Both schemes are equipped with a well-balancing (WB) property, which allows to preserve the equilibrium of *a priori* known stationary solutions exactly at the discrete level. We validate our numerical approaches by successfully reproducing standard vacuum test cases, such as the robust stability, the linearized wave, and the gauge wave tests, as well as achieving long-term stable evolutions of stationary black holes, including Kerr black holes with extreme spin. Concerning the coupling with matter, modeled by the relativistic Euler equations, we perform a classical test of spherical accretion onto a Schwarzschild black hole, as well as an evolution of a perturbed non-rotating neutron star, demonstrating the capability of our schemes to operate also on the full Einstein-Euler system. Altogether, these results provide a solid foundation for addressing more complex and challenging simulations of astrophysical sources through DG schemes on unstructured 3D meshes.

Keywords: Einstein field equations, relativistic Euler equations, Generalized Harmonic formulation, discontinuous Galerkin, non conservative, well-balancing

1. Introduction

When dealing with the numerical solution of the Einstein equations, both their mathematical formulation as a system of partial differential equations (PDEs) and their numerical discretization play a crucial role. At the moment, there are two main successful families of formulations of the Einstein equations that are routinely adopted for the simulation of astrophysical sources: those that are based on the 3+1 foliation of spacetime (see the monographies by [1], [16], [91], [68] for an overview), and those that belong to the Generalized Harmonic (GH) approach, which dates back to the origin of general relativity [40]. Within the 3+1 framework, after the seminal works by [94, 15], which gave birth to the so called BSSNOK formulation, there has been a steady effort over the years to obtain a better numerical control of the Einstein constraints. This has motivated the introduction of new versions such as Z4, CCZ4, Z4c, CFC [20, 21, 3, 4, 69, 36]. Within the GH framework, there has been continuous progress as well, which, not only allowed to perform

*Corresponding author

Email addresses: stefano.muzzolon@univr.it (Stefano Muzzolon), michael.dumbser@unitn.it (Michael Dumbser), olindo.zanotti@unitn.it (Olindo Zanotti), elena.gaburro@inria.fr (Elena Gaburro)

the first stable numerical simulation of a binary black hole merger [87], but also made it possible to go beyond the rigidity of the original GH prescription regarding the gauge condition [79].

If we look at the PDE structure of the two families of formulations, a fundamental feature emerges. While 3+1 formulations naturally arise as second-order (in space derivatives) PDE systems, GH formulations are easily written as first-order systems, which makes their hyperbolic nature much more cleaner and transparent to prove. This has strong implications on the choice of the numerical scheme that can be adopted for their solutions. In fact, one of the most promising numerical schemes, considered to be the frontier of numerical relativity (NR), is represented by discontinuous Galerkin (DG) schemes, which, notoriously, require a first-order formulation of the underlying PDEs. From this perspective, GH formulations are favored with respect to 3+1 second order formulations, and in fact DG schemes have already been successfully used for GH simulations, reaching a number of relevant scientific results [72, 100, 101, 42]. In general, the implementation of high order numerical schemes for first-order formulations of the Einstein equations is a fertile field of research. For example, within the 3+1 framework, a new first-order version of the BSSNOK formulation that could evolve a black hole binary system with different high order numerical schemes, including DG, has been recently proposed in [56, 54].

In this paper, we aim to give a contribution to the numerical discretization of the Einstein equations under the GH formulation, which consider various different perspectives. First, we introduce a Central WENO Finite Difference (CWENO-FD) scheme on Cartesian grids, which has been successfully used within the first-order version of the BSSNOK formulation [56], but has never been adopted in the GH formulation. Second, we introduce an ADER (Arbitrary high order Derivatives) discontinuous Galerkin (DG) scheme on 2D unstructured polygonal meshes, which should be regarded as a preliminary implementation towards a truly 3D numerical relativity calculation under the GH framework. Moreover, both numerical schemes are enriched by a well-balancing property, which allows to preserve the equilibrium of stationary (or quasi-stationary) configurations up to machine precision. This is an extra feature that can be activated according to user's needs and it follows closely the pragmatic approach proposed in [54].

The plan of the paper is the following. In Sect. 2 we recall the GH formulation of the Einstein equations; in Sect. 3 we describe the two numerical schemes adopted in the paper, while Sect. 4 contains the validation of our approach through a wide set of numerical tests. Finally, Sect. 5 presents the conclusions of our work.

We work in a geometrized set of units, in which the speed of light and the gravitational constant are set to unity, i.e., $c = G = 1$, and we assume $(-, +, +, +)$ as signature of the spacetime metric. Latin indices from the first part of the alphabet a, b, c, \dots denote spacetime indices ranging from 0 to 3, while Latin indices i, j, k, \dots are purely spatial, ranging from 1 to 3. We also use the Einstein summation convention of repeated indices.

2. Basic features of the GH formulation

We assume the spacetime to be foliated through $\Sigma_t = \text{const}$ hypersurfaces as

$$ds^2 = g_{ab} dx^a dx^b = -(\alpha^2 - \beta_i \beta^i) dt^2 + 2\beta_i dx^i dt + \gamma_{ij} dx^i dx^j, \quad (1)$$

where α is the lapse function, β^i is the shift vector and γ_{ij} is the metric of the three dimensional space, and where a natural observer is introduced with four velocity $n^a = (1/\alpha, -\beta^i/\alpha)$. However, unlike 3+1 formulations where each vector or tensor is decomposed along directions parallel and perpendicular to n^a , in the Generalized Harmonic (GH) framework the splitting expressed by (1) does not represent a constitutive feature. In fact, the GH formulation of the Einstein equations involves the full four-dimensional metric tensor g_{ab} and takes the first-order form [42]

$$\partial_t g_{ab} = (1 + \gamma_1) \beta^k \partial_k g_{ab} - \alpha \Pi_{ab} - \gamma_1 \beta^i \Phi_{iab}, \quad (2)$$

$$\begin{aligned}\partial_t \Phi_{iab} &= \beta^k \partial_k \Phi_{iab} - \alpha \partial_i \Pi_{ab} + \alpha \gamma_2 \partial_i g_{ab} + \frac{1}{2} \alpha n^c n^d \Phi_{icd} \Pi_{ab} \\ &\quad + \alpha \gamma^{jk} n^c \Phi_{ijc} \Phi_{kab} - \alpha \gamma_2 \Phi_{iab},\end{aligned}\tag{3}$$

$$\begin{aligned}\partial_t \Pi_{ab} &= \beta^k \partial_k \Pi_{ab} - \alpha \gamma^{ki} \partial_k \Phi_{iab} + \gamma_1 \gamma_2 \beta^k \partial_k g_{ab} \\ &\quad + 2\alpha g^{cd} (\gamma^{ij} \Phi_{ica} \Phi_{jdb} - \Pi_{ca} \Pi_{db} - g^{ef} \Gamma_{ace} \Gamma_{bdf}) \\ &\quad - 2\alpha \nabla_{(a} H_{b)} - \frac{1}{2} \alpha n^c n^d \Pi_{cd} \Pi_{ab} - \alpha n^c \Pi_{ci} \gamma^{ij} \Phi_{jab} \\ &\quad + \alpha \gamma_0 (2\delta^c_{(a} n_{b)} - g_{ab} n^c) C_c - \gamma_1 \gamma_2 \beta^i \Phi_{iab} - 16\pi \alpha \left(T_{ab} - \frac{1}{2} g_{ab} T^c_c \right),\end{aligned}\tag{4}$$

where we have used the definitions

$$\Phi_{iab} = \partial_i g_{ab}\tag{5}$$

$$\Pi_{ab} = -n^c \partial_c g_{ab}.\tag{6}$$

In Eqs. (2)–(4) three damping coefficients are present: γ_0 , which damps the 1-index or gauge constraint $C_a = H_a + \Gamma_a$; γ_1 , which controls the linear degeneracy of the system; γ_2 , which damps the 3-index constraint $C_{iab} = \partial_i g_{ab} - \Phi_{iab}$. Finally, Γ_{abc} are the spacetime Christoffel symbols of the first kind, i.e.,

$$\Gamma_{abc} = \frac{1}{2} (\partial_b g_{ac} + \partial_c g_{ab} - \partial_a g_{bc}), \quad \Gamma_a = g^{bc} \Gamma_{abc},\tag{7}$$

and H_a is a *gauge source function* which satisfies

$$H_a = g_{ab} \nabla_c \nabla^c x^b = -\Gamma_a.\tag{8}$$

During a typical simulation, we will constantly monitor the so-called *Einstein constraints*, given by

$$\mathcal{M}_a = \left(R_{ab} - \frac{1}{2} g_{ab} R - 8\pi T_{ab} \right) n^b = 0,\tag{9}$$

where

$$R_{ab} = g^{cd} g^{ef} (\partial_c g_{ae}) (\partial_d g_{bf}) - g^{ec} g^{fd} \Gamma_{aef} \Gamma_{bcd} - \frac{1}{2} g^{cd} (\partial_c \partial_d g_{ab}) + \nabla_{(a} \Gamma_{b)}, \quad R = g^{ab} R_{ab},\tag{10}$$

as well as the *gauge constraints*, given by

$$C_a = H_a + \Gamma_a.\tag{11}$$

It is also worth mentioning that the spatial components of Π_{ab} are related to the usual extrinsic curvature tensor adopted within the classical 3+1 formulation through

$$\Pi_{ij} = 2 K_{ij} + \frac{\beta^k}{\alpha} \partial_k \gamma_{ij} - \frac{1}{\alpha} (D_i \beta_j + D_j \beta_i),\tag{12}$$

where D_i represents the three-dimensional covariant derivative associated with the 3-metric γ_{ij} . In our setup, the matter-field content is given by a perfect fluid only, hence with an energy-momentum tensor of the form

$$T_{ab} = \rho h u_a u_b + p g_{ab},\tag{13}$$

where p is the gas pressure, ρ is the rest mass density and h is the specific (per unit mass) enthalpy, all of them measured in the comoving frame of the fluid with associated four velocity u^a . The latter is related

to v^i , the three velocity of the fluid as measured by the natural observer, by

$$u^i = W \left(v^i - \frac{\beta^i}{\alpha} \right), \quad (14)$$

where W is the Lorentz factor satisfying the relation

$$W = \frac{1}{\sqrt{1 - v^2}} = \alpha u^0, \quad (15)$$

with $v^2 = \gamma_{ij} v^i v^j$. The evolution equations for the fluid variables are the general relativistic Euler equations [14, 41, 91]

$$\partial_t (\sqrt{\gamma} D) + \partial_i (\sqrt{\gamma} (\alpha v^i D - \beta^i D)) = 0, \quad (16)$$

$$\partial_t (\sqrt{\gamma} S_j) + \partial_i (\sqrt{\gamma} (\alpha S^i_j - \beta^i S_j)) = \sqrt{\gamma} \left(\frac{\alpha}{2} S^{ik} \partial_j \gamma_{ik} + S_i \partial_j \beta^i - E \partial_j \alpha \right), \quad (17)$$

$$\partial_t (\sqrt{\gamma} E) + \partial_i (\sqrt{\gamma} (\alpha S^i - \beta^i E)) = \sqrt{\gamma} (\alpha S^{ij} K_{ij} - S^j \partial_j \alpha), \quad (18)$$

where γ is the determinant of γ_{ij} , S_{ij} is the spatial part of T_{ab} , and the remaining quantities in terms of the primitive physical variables read

$$D = \rho W, \quad S_i = \rho h W^2 v_i, \quad E = \rho h W^2 - p. \quad (19)$$

Using a compact vector notation, the Einstein-Euler equations in GH formulation can be written as first order hyperbolic system of balance laws

$$\frac{\partial \mathbf{u}}{\partial t} + \nabla \cdot \mathbf{F}(\mathbf{u}) + \mathbf{B}(\mathbf{u}) \cdot \nabla \mathbf{u} = \mathbf{S}(\mathbf{u}), \quad (20)$$

where the purely conservative term is only contributed by the matter part, whereas the Einstein sector is entirely written in non-conservative form. The state vector \mathbf{u} is composed of $54 + 5 = 59$ dynamical variables, i.e., 10 for the metric tensor g_{ab} , 10 for the tensor Π_{ab} , 30 for the tensor Φ_{tab} , 4 for the vector H_a and finally 5 for the matter part. Further details on the GH formulation can be found in [5, 79, 80].

3. The numerical scheme

In our work, we consider two distinct families of numerical schemes: the Central WENO Finite Difference (CWENO-FD) scheme on Cartesian grids, and the ADER (Arbitrary high order Derivatives) discontinuous Galerkin (DG) scheme on 2D unstructured polygonal meshes. In what follows, we provide an overview of the main concepts characterizing each of the two methods, including the techniques used to obtain the well-balancing property, which allows to preserve an *a priori* known equilibrium solution of the governing PDE system *exactly* at the discrete level. We recall that, since their first introduction by [18], well-balanced numerical methods have been extensively explored in the context of shallow water equations [74, 90, 7, 98], and, more generally, within the framework of hyperbolic balance laws [67, 86, 27, 64, 99, 85, 34, 17, 19], eventually finding applications in numerical relativity as well [62, 54, 11, 56]. For a more theoretical foundations of these methods, one can refer for instance to [32, 84, 33].

3.1. A well-balanced path-conservative CWENO finite difference scheme

Central WENO (CWENO) schemes were introduced in a series of seminal works for the numerical solutions of hyperbolic systems of conservation laws in [75, 76, 77] and in the context of finite volume schemes in [39, 93, 38, 104]. Their implementation is compatible with the more general framework of

conservative WENO finite-difference methods [95, 96, 70, 11], for which some extensions to nonlinear hyperbolic systems involving non-conservative products were proposed in [9, 10, 11], allowing for a broader range of applications, including numerical relativity. More recently, in the spirit of these studies, high order CWENO schemes have been successfully employed to tackle a novel first-order hyperbolic BSSNOK formulation, as presented in [56]. The interested reader can find in there a detailed description of this approach, which we briefly summarize below.

Central WENO reconstruction. We work with the discrete solution $\mathbf{u}_{i,j,k}$ of the system (20), evaluated at the cell centers of a uniform Cartesian grid. For ease of explanation, we limit the description of the procedure to the x direction only. Hence, discrete points are placed at

$$x_i = x_L + \frac{1}{2} \Delta x + (i-1) \Delta x, \quad \Delta x = \frac{x_R - x_L}{N_x}, \quad (21)$$

where x_L and x_R are the left and right boundaries of the computational domain, while N_x denotes the number of cells in that direction. We consider a large optimal stencil $\mathcal{S}_{opt} = \{i - \frac{N}{2}, \dots, i-1, i, i+1, \dots, i + \frac{N}{2}\}$, with $N > 2$ the degree of the reconstructed polynomial, and three smaller sub-stencils $\mathcal{S}_L = \{i-2, i-1, i\}$, $\mathcal{S}_C = \{i-1, i, i+1\}$, $\mathcal{S}_R = \{i, i+1, i+2\}$ for polynomials of lower degree. We express a generic polynomial of degree $M = M(k)$ on \mathcal{S}_k with respect to a set of polynomial basis functions $\mathbf{x} \mapsto \psi_m(x)$ as

$$P_k^M(x) = \sum_{m=0}^M \psi_m(x) \hat{u}_k^m, \quad \text{with} \quad k \in \{opt, L, C, R\}, \quad (22)$$

where the degrees of freedom \hat{u}_k^m are obtained by imposing conservation over cells,

$$\frac{1}{x_{j+\frac{1}{2}} - x_{j-\frac{1}{2}}} \int_{x_{j-\frac{1}{2}}}^{x_{j+\frac{1}{2}}} P_k^M(x) dx = u_j, \quad \forall j \in \mathcal{S}_k. \quad (23)$$

We compute an additional a priori unknown polynomial $P_0^N(x)$ from the optimal polynomial decomposition

$$P_{opt}^N(x) = \lambda_0 P_0^N(x) + \lambda_L P_L^2(x) + \lambda_C P_C^2(x) + \lambda_R P_R^2(x), \quad (24)$$

where $\lambda_0, \lambda_L, \lambda_C, \lambda_R$ are arbitrary linear weights, which we set to $\lambda_0 = 10^8$, $\lambda_C = 10^4$, and $\lambda_L = \lambda_R = 1$, as in [46]. We then use the standard WENO-type oscillation indicators σ_k

$$\sigma_k = \sum_{\alpha=1}^M \int_{x_{i-\frac{1}{2}}}^{x_{i+\frac{1}{2}}} \left(\frac{\partial^\alpha P_k^M(x)}{\partial x^\alpha} \right)^2 \Delta x^{2\alpha-1} dx, \quad \text{with} \quad k \in \{0, L, C, R\}, \quad (25)$$

to carry out a non-linear WENO reconstruction in terms of the polynomial $P_0^N(x)$ and of the lower degree polynomials, so that the final CWENO reconstruction is

$$w_h(x) = \sum_k \omega_k P_k^M(x), \quad \text{with} \quad k \in \{0, L, C, R\}, \quad (26)$$

where ω_k denote the nonlinear WENO weights

$$\omega_k = \frac{\tilde{\omega}_k}{\sum_m \tilde{\omega}_m}, \quad \text{with} \quad \tilde{\omega}_k = \frac{\lambda_k}{(\sigma_k + \epsilon)^r}, \quad (27)$$

and where we set $r = 4$ and $\epsilon = 10^{-7}$. See [56] for further details. To conclude, we evaluate $w_h(x)$ at the left and right interface of each interval defining $w_{i \pm \frac{1}{2}, j, k}^{\mp} = w_h(x_{i \pm \frac{1}{2}})$, and we use these reconstructed states to produce a high order accurate approximation of the first spatial derivative

$$\partial_x \mathbf{u}_{i, j, k} = \frac{\mathbf{w}_{i+\frac{1}{2}, j, k}^- - \mathbf{w}_{i-\frac{1}{2}, j, k}^+}{\Delta x}. \quad (28)$$

This type of reconstruction is repeated for the discrete derivatives along the y and the z directions, to obtain the discrete spatial gradient $\nabla \mathbf{u}_{i, j, k}$, and it is also applied to the point values of the fluxes, again in each direction.

CWENO-FD discretization. The semi-discrete path-conservative FD scheme for system (20) then reads

$$\begin{aligned} \frac{d\mathbf{u}_{i, j, k}}{dt} = & -\frac{\mathbf{f}_{i+\frac{1}{2}, j, k}^x - \mathbf{f}_{i-\frac{1}{2}, j, k}^x}{\Delta x} - \frac{\mathbf{f}_{i, j+\frac{1}{2}, k}^y - \mathbf{f}_{i, j-\frac{1}{2}, k}^y}{\Delta y} - \frac{\mathbf{f}_{i, j, k+\frac{1}{2}}^z - \mathbf{f}_{i, j, k-\frac{1}{2}}^z}{\Delta z} - \mathbf{B}(\mathbf{u}_{i, j, k}) \cdot \nabla \mathbf{u}_{i, j, k} + \\ & -\frac{\mathbf{D}_{i+\frac{1}{2}, j, k}^x + \mathbf{D}_{i-\frac{1}{2}, j, k}^x}{\Delta x} - \frac{\mathbf{D}_{i, j+\frac{1}{2}, k}^y + \mathbf{D}_{i, j-\frac{1}{2}, k}^y}{\Delta y} - \frac{\mathbf{D}_{i, j, k+\frac{1}{2}}^z + \mathbf{D}_{i, j, k-\frac{1}{2}}^z}{\Delta z} + \mathbf{S}(\mathbf{u}_{i, j, k}), \end{aligned} \quad (29)$$

where $\partial_x \mathbf{u}_{i, j, k}$ is determined using the CWENO reconstruction reported above, and the numerical fluxes are obtained through a Rusanov-type Riemann solver. The jump terms involving \mathbf{D}^x , which do not appear in traditional central FD schemes, affect the order of accuracy and the robustness of the overall method, see [11]. For the Rusanov-type scheme that we adopt, they are defined as

$$\mathbf{D}_{i+\frac{1}{2}, j, k}^x = \frac{1}{2} \tilde{\mathbf{B}}_{i+\frac{1}{2}, j, k}^x \cdot \left(\mathbf{w}_{i+\frac{1}{2}, j, k}^+ - \mathbf{w}_{i+\frac{1}{2}, j, k}^- \right), \quad (30)$$

where we use a simple midpoint rule for the $\tilde{\mathbf{B}}^x$ term, namely $\tilde{\mathbf{B}}_{i+\frac{1}{2}, j, k}^x = \mathbf{B}^x \left(\frac{1}{2} (\mathbf{w}_{i+\frac{1}{2}, j, k}^+ + \mathbf{w}_{i+\frac{1}{2}, j, k}^-) \right)$. The numerical flux reads

$$\mathbf{f}_{i+\frac{1}{2}, j, k}^x = \frac{1}{2} \left(\mathbf{f}_{i+\frac{1}{2}, j, k}^{x,-} + \mathbf{f}_{i+\frac{1}{2}, j, k}^{x,+} \right) - \frac{1}{2} \lambda_{i+\frac{1}{2}, j, k}^{\max} \left(\mathbf{w}_{i+\frac{1}{2}, j, k}^+ - \mathbf{w}_{i+\frac{1}{2}, j, k}^- \right), \quad (31)$$

with $\lambda_{i+\frac{1}{2}, j, k}^{\max}$ an estimate of the maximum wave speed at the interface. Analogous formulae are used in the y and z directions, respectively.

For the temporal integration, we employ classical or TVD Runge-Kutta schemes of sufficiently high order of accuracy, consistent with the spatial discretization.

Well-balancing of the final CWENO-FD scheme. To make the numerical scheme well-balanced, we follow the approach described in [54], which is in turn inspired by [66, 85, 17]. The procedure is in principle quite simple: we subtract the equilibrium solution from the governing PDE system, thus removing the discretization errors introduced by the numerical scheme in the vicinity of the equilibrium. In other words, if $\mathbf{u}_e = \mathbf{u}_e(x, y, z)$ denotes a stationary equilibrium solution, that is $\partial_t \mathbf{u}_e = 0$, we subtract Eq. (20) evaluated at \mathbf{u}_e from its general form, thus obtaining

$$\frac{\partial \mathbf{u}}{\partial t} + \nabla \cdot \mathbf{F}(\mathbf{u}) - \nabla \cdot \mathbf{F}(\mathbf{u}_e) + \mathbf{B}(\mathbf{u}) \cdot \nabla \mathbf{u} - \mathbf{B}(\mathbf{u}_e) \cdot \nabla \mathbf{u}_e = \mathbf{S}(\mathbf{u}) - \mathbf{S}(\mathbf{u}_e). \quad (32)$$

We then rewrite the latter into an augmented form by introducing a new vector variable $\tilde{\mathbf{u}} = [\mathbf{u}, \mathbf{u}_e]^T$, which is evolved by the code, and suitable extensions of the operators involved. We finally remark that one has to modify appropriately also the structure of the numerical viscosity in the Rusanov-type Riemann solver. See [54] for more details.

3.2. A well-balanced path-conservative ADER discontinuous Galerkin scheme

The ADER approach was first introduced in [103] as a fully-discrete one-step procedure to achieve arbitrary high order of accuracy in both space and time. As shown in [89, 52, 65], it can be framed within the context of discontinuous Galerkin (DG) finite element methods, leading to the so called ADER-DG schemes. Its modern formulation [48, 45], which consists in using a local predictor-corrector technique, has demonstrated remarkable effectiveness and versatility on many different PDE systems [53, 47, 51, 44, 13, 12, 57, 107], including some applications to general relativity [50, 49, 62, 55]. In addition, it has also been extended to the Arbitrary-Lagrangian-Eulerian (ALE) framework on general unstructured polygonal meshes [23, 24, 26, 25, 59, 61]. The latter is the setting that we assume here, although in the present paper we limit our attention to a fixed mesh configuration, leaving the much more challenging case of moving meshes with topology changes [97, 61, 63] to a future work.

Data representation. We consider a 2D domain covered by an unstructured mesh of non-overlapping polygons P_i^n , $i = 1, \dots, N_P$ (see Figure 1 for a representative illustration), that could be in principle rearranged at each time step t^n , where the vector variable \mathbf{u} for Eq. (20) is represented by a piecewise polynomial of degree N ,

$$\mathbf{u}_h^n(\mathbf{x}, t^n) = \sum_{\ell=0}^{N-1} \varphi_\ell(\mathbf{x}, t^n) \hat{\mathbf{u}}_{\ell,i}^n, \quad \mathbf{x} \in P_i^n, \quad (33)$$

with $\mathbf{x} \mapsto \varphi_\ell(\mathbf{x}, t^n)$ local modal spatial basis functions, and $N = \mathcal{L}(N, 2)$ where $\mathcal{L}(N, d) = \frac{1}{d!} \prod_{m=1}^d (N+m)$. In practice, to determine the total number of elements N_P in the typical case of a rectangular domain, we fix a desired approximate number of elements in the x direction N_x , and we then compute an optimal number of elements in the y direction N_y , to ensure the resulting mesh is as uniform as possible. Consequently, in the numerical tests, we will use N_x as an indicative measure of the mesh resolution as it directly controls the refinement process.

We remark that, although in the DG framework there is no need to use spatial reconstruction techniques as expression (33) provides already an $N+1$ -order accurate data representation in space, we anyway rename $\mathbf{w}_h^n(\mathbf{x}, t^n) = \mathbf{u}_h^n(\mathbf{x}, t^n)$ to follow the conventional notation adopted in the majority of the references mentioned above.

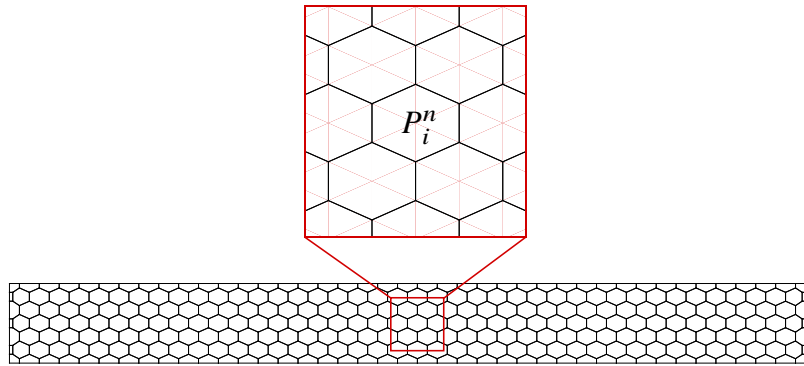


Figure 1: An example of a rectangular 2D unstructured mesh covered by non-overlapping polygons P_i^n . Above, a zoomed-in portion highlights the polygonal structure.

The space-time predictor. The main ingredient of the method is a *local* procedure consisting in solving a weak form of the governing PDE system to obtain a *predictor* \mathbf{q}_h^n of the solution for each element, which is a space-time polynomial of degree N described by

$$\mathbf{q}_h^n(\mathbf{x}, t) = \sum_{\ell=0}^{Q-1} \theta_\ell(\mathbf{x}, t) \hat{\mathbf{q}}_\ell^n, \quad (\mathbf{x}, t) \in C_i^n, \quad (34)$$

where $(\mathbf{x}, t) \mapsto \theta_\ell(\mathbf{x}, t)$ are modal space-time basis functions, $Q = \mathcal{L}(N, 3)$, and C_i^n is the space-time control volume bounded by the elements P_i^n and P_i^{n+1} . In more detail, we multiply the PDE system (20) by time-dependent test functions $(\mathbf{x}, t) \mapsto \theta_k(\mathbf{x}, t)$ and we integrate over C_i^n , obtaining

$$\begin{aligned} & \int_{C_i^n} \theta_k(\mathbf{x}, t) \frac{\partial \mathbf{q}_h^n}{\partial t} d\mathbf{x} dt + \int_{C_i^n} \theta_k(\mathbf{x}, t) (\nabla \cdot \mathbf{F}(\mathbf{q}_h^n) + \mathbf{B}(\mathbf{q}_h^n) \cdot \nabla \mathbf{q}_h^n) d\mathbf{x} dt \\ &= \int_{C_i^n} \theta_k(\mathbf{x}, t) \mathbf{S}(\mathbf{q}_h^n) d\mathbf{x} dt, \quad \forall k \in \{0, \dots, Q-1\}. \end{aligned} \quad (35)$$

We then insert the known discrete solution $\mathbf{w}_h^n(\mathbf{x}, t^n)$ at time t^n and we integrate by parts the first term in time, finding

$$\begin{aligned} & \int_{P_i^{n+1}} \theta_k(\mathbf{x}, t^{n+1}) \mathbf{q}_h^n(\mathbf{x}, t^{n+1}) d\mathbf{x} - \int_{P_i^n} \theta_k(\mathbf{x}, t^n) \mathbf{w}_h^n(\mathbf{x}, t^n) d\mathbf{x} - \int_{C_i^n} \frac{\partial}{\partial t} \theta_k(\mathbf{x}, t) \mathbf{q}_h^n(\mathbf{x}, t) d\mathbf{x} dt \\ &+ \int_{C_i^n \setminus \partial C_i^n} \theta_k(\mathbf{x}, t) \nabla \cdot \mathbf{F}(\mathbf{q}_h^n) d\mathbf{x} dt = \int_{C_i^n \setminus \partial C_i^n} \theta_k(\mathbf{x}, t) (\mathbf{S}(\mathbf{q}_h^n) - \mathbf{B}(\mathbf{q}_h^n) \cdot \nabla \mathbf{q}_h^n) d\mathbf{x} dt, \quad \forall k \in \{0, \dots, Q-1\}, \end{aligned} \quad (36)$$

which leads to an element-local nonlinear system for the degrees of freedom $\hat{\mathbf{q}}_\ell^n$, that we solve via a discrete Picard iteration [48, 106], for which convergence was proven in [31].

The corrector step. We start by rewriting Eq. (20) in a space-time divergence form,

$$\tilde{\nabla} \cdot \tilde{\mathbf{F}}(\mathbf{u}) + \tilde{\mathbf{B}}(\mathbf{u}) \cdot \tilde{\nabla} \mathbf{u} = \mathbf{S}(\mathbf{u}), \quad \text{with } \tilde{\mathbf{F}} = (\mathbf{u}, \mathbf{F}), \quad \tilde{\mathbf{B}} = (\mathbf{0}, \mathbf{B}), \quad \text{and } \tilde{\nabla} = (\partial_t, \partial_{\mathbf{x}})^T. \quad (37)$$

We then multiply it by so-called moving test functions $(\mathbf{x}, t) \mapsto \tilde{\varphi}_k(\mathbf{x}, t)$, which coincide with the basis function of Eq. (33) at $t = t^n$ and at $t = t^{n+1}$, i.e. $\tilde{\varphi}_k(\mathbf{x}, t^n) = \varphi_k(\mathbf{x}, t^n)$ and $\tilde{\varphi}_k(\mathbf{x}, t^{n+1}) = \varphi_k(\mathbf{x}, t^{n+1})$ and automatically adapt to an eventual moving mesh framework. Next, we integrate over each C_i^n applying the Gauss theorem to the flux-divergence term and splitting the non-conservative products into volume and surface contribution, to obtain

$$\begin{aligned} & \int_{P_i^{n+1}} \tilde{\varphi}_k \mathbf{u}_h(\mathbf{x}, t^{n+1}) d\mathbf{x} = \int_{P_i^n} \tilde{\varphi}_k \mathbf{u}_h(\mathbf{x}, t^n) d\mathbf{x} - \sum_{j=1}^{N_{V_i}^{n,st}} \int_{\partial C_{ij}^n} \tilde{\varphi}_k \mathcal{D}(\mathbf{q}_h^{n,-}, \mathbf{q}_h^{n,+}) \cdot \tilde{\mathbf{n}} dS \\ &+ \int_{C_i^n \setminus \partial C_i^n} \tilde{\nabla} \tilde{\varphi}_k \cdot \tilde{\mathbf{F}}(\mathbf{q}_h^n) d\mathbf{x} dt + \int_{C_i^n \setminus \partial C_i^n} \tilde{\varphi}_k(\mathbf{x}, t) (\mathbf{S}(\mathbf{q}_h^n) - \mathbf{B}(\mathbf{q}_h^n) \cdot \nabla \mathbf{q}_h^n) d\mathbf{x} dt, \quad \forall k \in \{0, \dots, \mathcal{N}-1\}, \end{aligned} \quad (38)$$

where $N_{V_i}^{n,st}$ is the number of spacetime neighbors, $\tilde{\mathbf{n}} = (\tilde{n}_t, \tilde{\mathbf{n}}_{\mathbf{x}})$ denotes the outward pointing spacetime unit normal vector on the faces composing the boundary of C_i^n , the $\tilde{\mathbf{F}}$ -term is simply the physical space-time flux evaluated at the discrete solution \mathbf{q}_h and the \mathcal{D} -term is a path-conservative Rusanov-type fluctuation that reads

$$\mathcal{D}(\mathbf{q}_h^{n,-}, \mathbf{q}_h^{n,+}) \cdot \tilde{\mathbf{n}} = \frac{1}{2} (\tilde{\mathbf{F}}(\mathbf{q}_h^+) - \tilde{\mathbf{F}}(\mathbf{q}_h^-)) \cdot \tilde{\mathbf{n}} + \frac{1}{2} \bar{\mathbf{B}} \cdot (\mathbf{q}_h^+ - \mathbf{q}_h^-) - \frac{1}{2} s_{\max} (\mathbf{q}_h^+ - \mathbf{q}_h^-). \quad (39)$$

Here, $\mathbf{q}_h^{n,-}$ and $\mathbf{q}_h^{n,+}$ are the boundary-extrapolated data from the predictor in each shared lateral surface ∂C_{ij}^n , s_{\max} is an estimate for the maximum signal speed at the cell interface and the average matrix $\bar{\mathbf{B}}$ is computed according to a path integral along a straight-line segment path as follows:

$$\bar{\mathbf{B}} = \int_0^1 \tilde{\mathbf{B}}(\psi(\xi)) d\xi, \quad \psi = \mathbf{q}_h^- + \xi(\mathbf{q}_h^+ - \mathbf{q}_h^-). \quad (40)$$

Eq. (38) provides the final update from t^n to t^{n+1} , since the unknown $\mathbf{u}_h(\mathbf{x}, t^{n+1})$ can be computed from the solution at the previous time step, $\mathbf{u}_h(\mathbf{x}, t^n)$ by exploiting the predictor $\mathbf{q}_h(\mathbf{x}, t)$ when computing the various integrals appearing in the formulation.

Well-balancing of the final ADER-DG scheme. For the well-balancing of the scheme, we refer to the approach recently precisely described in [60] and references therein. The underlying idea is to consider three groups of quantities: the equilibrium solution \mathbf{u}_e , which exactly satisfies the PDE system (20); the *fluctuation* \mathbf{u}_f , which accounts for the deviations from the equilibrium profile and is also represented following Eq. (33); and the complete numerical solution \mathbf{u}_h , which corresponds to the variable involved in the original (non well-balanced) version of the scheme, that however here takes the form

$$\mathbf{u}_h(\mathbf{x}, t) = \mathbf{u}_e(\mathbf{x}, t) + \mathbf{u}_f(\mathbf{x}, t), \quad (41)$$

accounting for both the contributions of the equilibrium and its fluctuations. Based on these definitions, we proceed as follows. We first subtract the predictor equation (36) evaluated at the equilibrium \mathbf{u}_e , to Eq. (36) itself, obtaining a system that characterizes the predictor for the fluctuation \mathbf{q}_f , which we solve using a fixed point iteration as before. We then use the same subtraction strategy for the corrector equation (38) to derive an update formula for the degrees of freedom of the fluctuation \mathbf{u}_f , which completes our WB algorithm. As a final remark on the well-balanced structure of the scheme, we notice that the predictor \mathbf{q}_h to be used inside the WB corrector formula should be obtained by summing up the equilibrium solution to the computed predictor of the fluctuation $\mathbf{q}_h(\mathbf{x}, t) = \mathbf{u}_e(\mathbf{x}, t) + \mathbf{q}_f(\mathbf{x}, t)$.

4. Numerical tests

In this Section, we present an extensive set of standard test cases in numerical relativity to assess the accuracy and robustness of the two numerical methods proposed in Sect. 3, namely the CWENO Finite Difference and ADER discontinuous Galerkin schemes, applied to the first-order hyperbolic Generalized Harmonic (GH) formulation of the Einstein-Euler system. In particular, the vacuum spacetime setups are taken from the widely used and well-established benchmark tests provided in [2]. In what follows, we briefly describe each test case and analyze the effectiveness of our numerical approaches, especially in achieving long-term stable simulations, which, unless otherwise specified, are all performed up to the canonical final time of $t = 1000$. To this end, we monitor the time evolution of the Einstein and gauge constraints given by Eqs. (9) and (11), and referring to their components as $M0, M1, M2, M3$, and $C0, C1, C2, C3$, respectively. We remark that, throughout all the tests, we show only the distinct components of the constraints when some coincide, and we omit from the plots any components that vanish identically. We also mention that we consider the components of the gauge source function H_a to be fixed once specified on the initial data, even though one could provide evolution equations also for them if necessary [87, 88, 78]. Finally, notice that in the tests where a matter-field is present, we convert the conservative variables given in Eq. (19) back to the primitive variables (ρ, v_i, p) following closely the procedure detailed in [54].

4.1. The robust stability test

A first validation procedure for numerical relativity codes is the so called *robust stability test*, as described in [2]. This test is designed to identify potential exponentially growing modes that could otherwise

remain hidden for an extended evolution time, and therefore it is used to empirically verify the hyperbolicity of the governing system of equations. It is performed in a flat Minkowski spacetime without matter and it consists of applying small independent random perturbations to each evolved quantity of the PDE system. The amplitude of the perturbation is $\pm 10^{-7}/\varrho^2$, where the parameter $\varrho \in \{1, 2, 4\}$ serves as mesh refinement factor. We underline that the chosen amplitude is three orders of magnitude larger than the one reported in [2], producing in this way an even more challenging configuration. The computational domain is given by the unit square $\Omega = [-0.5, 0.5] \times [-0.5, 0.5]$, which is discretized setting $N_x = 10\varrho$ for the ADER-DG schemes, and by $50\varrho \times 50\varrho$ grid points for the CWENO-FD schemes. At the boundary, we impose flat Minkowski spacetime. In Figure 2 we show the evolution of the constraints for two sets of simulations, where we employ a fourth order ADER-DG and a fifth order CWENO-FD scheme. Here, no damping is used, i.e., we choose $\gamma_0 = \gamma_1 = \gamma_2 = 0$. Moreover, we evolve the data in *harmonic gauge*, setting $H_a = 0$ everywhere. For a complete analysis, it is interesting to compare these results with those obtained using other first-order hyperbolic versions of well-known formulations, such as the Z4 system presented in [54], and the BSSNOK system detailed in [56].

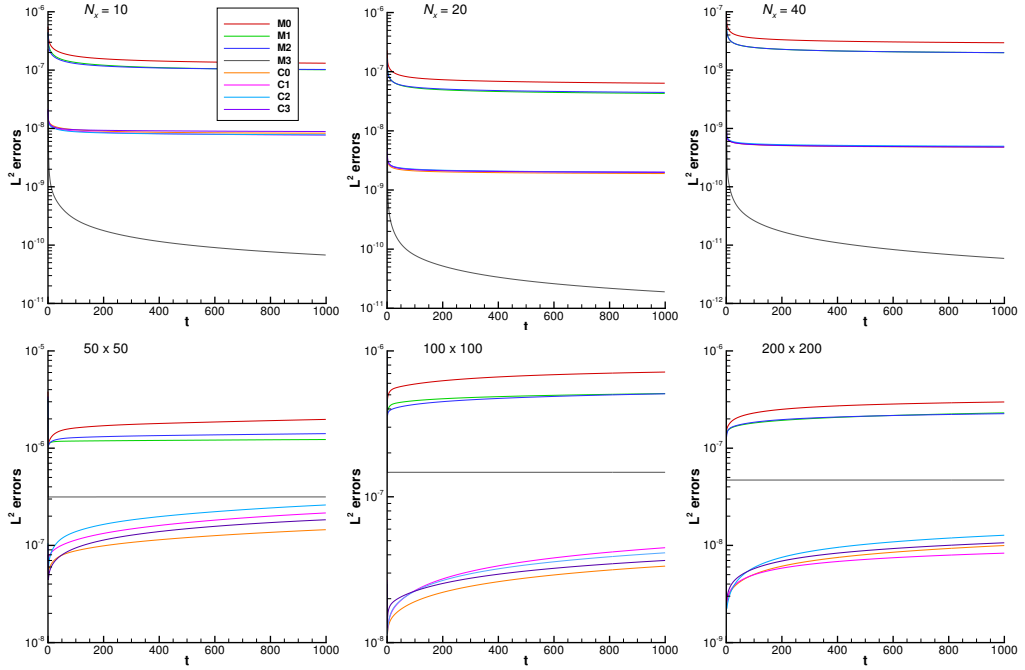


Figure 2: Time evolution of the constraints for the robust stability test case with a random initial perturbation of amplitude $\pm 10^{-7}/\varrho^2$ applied to all variables, performed on a sequence of successively refined meshes on the unit square in 2D. Top panel from left to right: fourth order ADER-DG scheme with $10 (\varrho = 1)$, $20 (\varrho = 2)$, and $40 (\varrho = 4)$ elements in the x direction. Bottom panel from left to right: fifth order CWENO-FD scheme on $50 \times 50 (\varrho = 1)$, $100 \times 100 (\varrho = 2)$, and $200 \times 200 (\varrho = 4)$ grid points.

4.2. The linearized gravitational wave

The *linearized gravitational wave* is essentially a one-dimensional test, consisting of a small gravitational wave perturbation of the flat Minkowski spacetime without matter, for which the metric results in

$$ds^2 = -dt^2 + dx^2 + (1 + b) dy^2 + (1 - b) dz^2, \quad \text{with} \quad b = \epsilon \sin(2\pi(x - t)), \quad (42)$$

where $\epsilon = 10^{-8}$. This choice ensures that the model dynamics is linear and the terms depending on ϵ^2 can be neglected. As described in [2], this test is used to check the ability of a code to propagate a travelling gravitational wave, revealing possible sources of inaccuracy in the algorithms adopted.

The components of the spatial metric can be readily identified from Eq. (42) as $\gamma_{11} = 1$, $\gamma_{22} = 1 + b$, and $\gamma_{33} = 1 - b$, as well as the ones of the shift vector, $\beta^i = 0$, and the value of the lapse function, $\alpha = 1$. Other relevant non-zero quantities worth mentioning are Π_{22} and Π_{33} , due to their direct relation with the extrinsic curvature K_{ij} , which in the no-shift case reduces to $\Pi_{ij} = 2K_{ij}$, see Eq. (12). We consider a rectangular domain $\Omega = [-0.5, 0.5] \times [-0.05, 0.05]$ with periodic boundary conditions in both directions, and we use the *harmonic gauge condition* $H_a = 0$, while all damping parameters are set to zero.

In Figure 3 we present the results obtained with the ADER-DG scheme of order four on a mesh where $N_x = 60$. In particular, we monitor the time evolution of the constraints, and we report the profile of the variable Π_{22} over the entire 2D domain Ω , together with a one-dimensional cut that is compared against the exact solution.

Since the CWENO-FD schemes provide results similar to those of Figure 3, we omit the corresponding plots. Instead, in Table 1, we perform a numerical convergence analysis at short time $t = 1$ to show that they achieve the expected order of accuracy.

In all the following convergence tables, we will use the notation \mathbb{P}_N to denote, in the CWENO-FD case, the schemes obtained by reconstructing an optimal polynomial of degree N , see Eq. (24), while in the ADER-DG case, the schemes obtained by representing the discrete solution by piecewise polynomials of degree N , see Eq. (33).

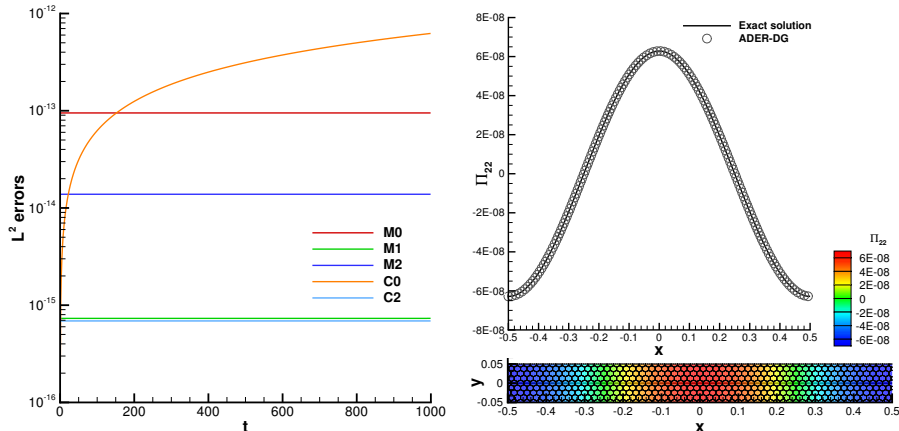


Figure 3: Solution of the linearized wave test using the fourth order ADER-DG scheme on an unstructured polygonal mesh. Left panel: time evolution of the constraints. Right panel: below, 2D color contour of Π_{22} ; above, comparison of the exact and numerical solution at final time $t = 1000$ on a one dimensional cut at $y = 0$.

4.3. The gauge wave

Another significant test taken from [2] is the so called *gauge wave test*, which involves the evolution of a propagating wave on a flat Minkowski spacetime with a time-dependent spatial metric. A common choice, which we adopt here, is to consider a sinusoidal profile of amplitude A propagating along the x -axis, leading to

$$ds^2 = -H(x, t) dt^2 + H(x, t) dx^2 + dy^2 + dz^2, \quad \text{where} \quad H(x, t) = 1 - A \sin(2\pi(x - t)). \quad (43)$$

Consequently, we have $\gamma_{11} = H$ and $\gamma_{22} = \gamma_{33} = 1$, with no shift, i.e. $\beta^i = 0$, and a time-dependent lapse function $\alpha = \sqrt{H}$. The only non-zero components of the tensor Π_{ab} are Π_{00} and Π_{11} , where $\Pi_{00} = -\Pi_{11}$

Scheme	$N_x \times N_y$	L^2 Error Π_{22}	$O(\Pi_{22})$	Theoretical
CWENO-FD \mathbb{P}_4	8×8	3.9347E-10	-	5.00
	16×16	1.3403E-11	4.88	
	24×24	1.7898E-12	4.97	
CWENO-FD \mathbb{P}_6	8×8	5.0194E-11	-	7.00
	16×16	4.3791E-13	6.84	
	24×24	2.6151E-14	6.95	
CWENO-FD \mathbb{P}_8	10×10	9.4470E-13	-	9.00
	16×16	1.4826E-14	8.84	
	24×24	3.9615E-16	8.93	

Table 1: Numerical convergence results for the linearized wave test at $t = 1$ for the variable Π_{22} using the CWENO-FD schemes.

with

$$\Pi_{11} = -2\pi A \frac{\cos(2\pi(x-t))}{\sqrt{1 - A \sin(2\pi(x-t))}}. \quad (44)$$

We run our tests over a rectangular domain $\Omega = [-0.5, 0.5] \times [-0.05, 0.05]$ with periodic boundary conditions in both directions. Moreover, we again use the *harmonic gauge condition* $H_a = 0$, and no damping whatsoever, that is, $\gamma_0 = \gamma_1 = \gamma_2 = 0$.

At first glance, there seems to be no reason to consider this test particularly challenging. However, it is well-documented that its successful resolution is, in fact, quite involved. Although it depends on the specific formulation under analysis, difficulties typically become evident at high amplitude, i.e. $A = 0.1$. This is the case for the BSSNOK system, which fails after a rather short time in both its first and second order classical formulations, as described in [3, 29]. The original version of the CCZ4 system is stable only in its damped formulation [3], whereas the first-order formulation FO-CCZ4 presented in [50] provided the first stable undamped simulation with CCZ4. Conversely, this test can be effectively handled within the Z4 formulation [54] as well as the GH formulation [8, 28, 81], which is the object of study in this paper.

We first perform a simulation with large amplitude $A = 0.1$ using the fifth order CWENO-FD scheme on a 64×16 grid, with corresponding results presented in Figure 4. We then run a second simulation with an even higher amplitude $A = 0.5$ employing the fourth order ADER-DG method on a mesh generated by $N_x = 60$ elements in the x direction, as shown in Figure 5. In both cases, we notice that the constraints remain controlled throughout the time evolution, and the exact profile of the variable g_{00} is perfectly recovered at the final time $t = 1000$, suggesting that both tests are well resolved.

To conclude our study, in Tables 2 and 3 we present a numerical convergence analysis at time $t = 1$ and high amplitude $A = 0.5$ for the CWENO-FD and ADER-DG schemes, respectively. In the latter case, we also provide the maximum diameter h of the circumcircles over all elements as an additional characteristic measure of the mesh size.

4.4. Single stationary black holes in two and three space dimensions

The first exact nontrivial solution of the Einstein equations is the *Schwarzschild metric*, derived by Karl Schwarzschild [92] shortly after Einstein published his foundational paper on the theory of general relativity. It describes the spacetime surrounding a static, spherically symmetric object, such as a non-rotating black hole. Then, almost fifty years had to pass before a generalization to rotating, stationary, axially symmetric black holes was proposed by Roy Kerr [71], reflecting the difficulties of its derivation. This solution is known as the *Kerr metric*.

Throughout the simulations reported here, the black hole mass is chosen as $M = 1 M_\odot$, and T_{ab} vanishes since we are indeed dealing with vacuum solutions. Moreover, we remark that the 2D tests are performed

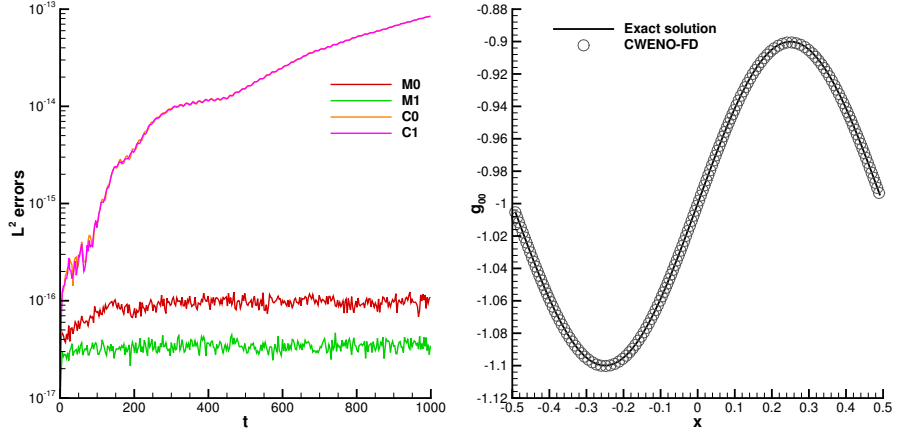


Figure 4: Solution of the gauge wave test with amplitude $A = 0.1$ using the fifth order CWENO-FD scheme on a Cartesian mesh. Left panel: time evolution of the constraints. Right panel: comparison of the exact and numerical solution for the variable g_{00} at final time $t = 1000$ on a one dimensional cut at $y = 0$.

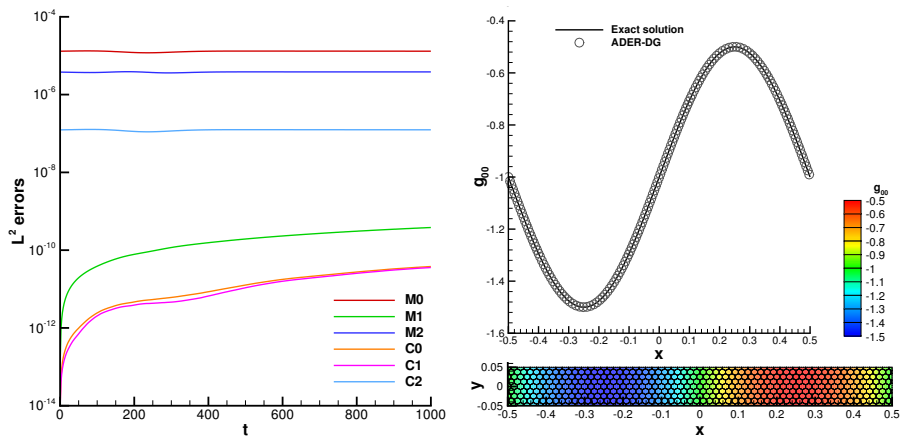


Figure 5: Solution of the gauge wave test with high amplitude $A = 0.5$ using the fourth order ADER-DG scheme on an unstructured polygonal mesh. Left panel: time evolution of the constraints. Right panel: below, 2D color contour of g_{00} ; above, comparison of the exact and numerical solution at final time $t = 1000$ on a one dimensional cut at $y = 0$.

Scheme	$N_r \times N_\theta$	L^2 Error g_{00}	$O(g_{00})$	Theoretical
CWENO-FD \mathbb{P}_4	32×32	1.3335E-05	-	
	64×64	4.5713E-07	4.87	5.00
	96×96	6.1146E-08	4.96	
CWENO-FD \mathbb{P}_6	32×32	1.6025E-06	-	
	64×64	1.5767E-08	6.67	7.00
	96×96	9.6039E-10	6.90	
CWENO-FD \mathbb{P}_8	32×32	3.4042E-07	-	
	64×64	1.0864E-09	8.29	9.00
	96×96	3.8951E-11	8.21	

Table 2: Numerical convergence results for the gauge wave test with high amplitude $A = 0.5$ at $t = 1$ for the variable g_{00} using the family of CWENO-FD schemes on Cartesian grids.

Scheme	N_x	h	L^2 Error g_{00}	$O(g_{00})$	Theoretical
ADER-DG \mathbb{P}_1	40	8.3140E-03	1.7907E-04	-	
	80	4.4844E-03	4.4628E-05	2.25	2.00
	120	3.0898E-03	2.0248E-05	2.12	
ADER-DG \mathbb{P}_2	40	8.3140E-03	2.0386E-06	-	
	80	4.4844E-03	2.6027E-07	3.33	3.00
	120	3.0898E-03	7.7873E-08	3.24	
ADER-DG \mathbb{P}_3	40	8.3140E-03	1.5630E-08	-	
	80	4.4844E-03	1.0416E-09	4.39	4.00
	120	3.0898E-03	2.0965E-10	4.30	
ADER-DG \mathbb{P}_4	20	2.0127E-02	5.5749E-09	-	
	40	8.3140E-03	1.7908E-10	3.89	5.00
	80	4.4844E-03	9.9518E-12	4.68	

Table 3: Numerical convergence results for the gauge wave test with high amplitude $A = 0.5$ at $t = 1$ for the variable g_{00} using the family of ADER-DG schemes on unstructured polygonal meshes.

using the ADER-DG scheme, while for the 3D ones the CWENO-FD method is employed instead.

Non-rotating black hole in 2D. We begin by evolving a Schwarzschild black hole ($a = 0$) in Boyer-Lindquist coordinates (see, for instance, Appendix B of [73], or the more extended discussion on the different coordinate systems adapted to the Kerr spacetime in [105]). The two-dimensional computational domain $(r, \theta) \in [2.5, 5] \times [\delta, \pi - \delta]$, with $\delta = 0.520796327$, is discretized by 50 elements in the r direction, namely setting $N_x = 50$. At both boundaries, we impose Dirichlet boundary condition for all variables, using the initial configuration. The gauge source function H_a is computed directly from the analytical initial data as $H_a = -\Gamma_a$, and we set the damping parameters to $\gamma_0 = \gamma_2 = 1, \gamma_1 = -1$. We introduce a *small Gaussian perturbation* on the g_{00} component of the initial spacetime metric with the aim of studying the well-balancing property of the scheme. More precisely, at time $t = 0$, we set

$$\tilde{g}_{00}(r, \theta) = g_{00}(r, \theta) + A \exp\left(-\frac{1}{2} \frac{(r \sin \theta - 4)^2 + (r \cos \theta - 0)^2}{\sigma^2}\right), \quad (45)$$

with $A = 10^{-4}$ and $\sigma = 0.2$. We present the results obtained with the well-balanced fourth order version of the ADER-DG scheme in Figure 6. In line with our expectations, the perturbation gradually propagates out of the domain, so that at sufficiently large time the solution returns to the exact stationary equilibrium state.

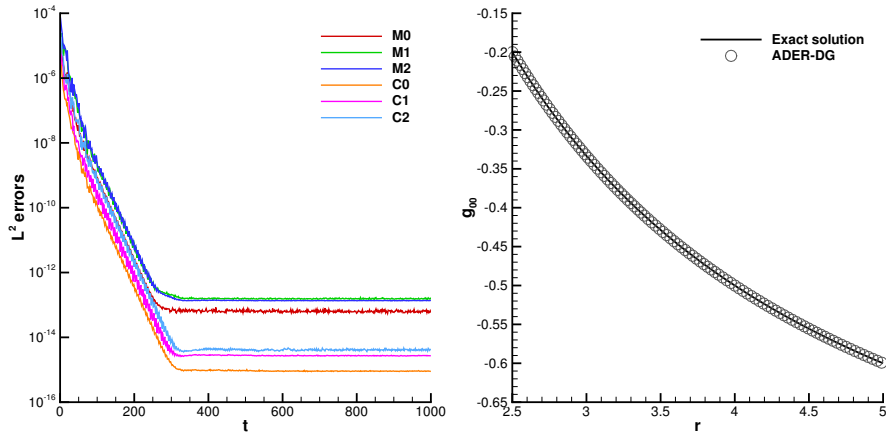


Figure 6: 2D Schwarzschild black hole subject to an initial Gaussian perturbation in the variable g_{00} using the well-balanced fourth order ADER-DG scheme. Left panel: time evolution of the constraints, which decay after a relatively short period of time. Right panel: comparison of the exact and numerical solution for the variable g_{00} at final time $t = 1000$ on a one dimensional cut at $\theta = \pi/2$.

We then provide a further setup, in which we fully exploit the ability of our ADER-DG code to operate on general unstructured polygonal meshes. To this end, we evolve a Schwarzschild black hole using the 3D Cartesian horizon-penetrating harmonic coordinates (t, x, y, z) described in SPECTRE documentation [43], which are in turn based on [35]. To perform a 2D simulation, however, we restrict our attention to the evolution of the solution over the equatorial plane $z = 0$. We emphasize that, in this configuration, we need to take special care of the z direction by introducing an artificial source term in Eq. (20) to account for possible non-zero terms arising from derivatives of the state variables with respect to the z coordinate. This passage is in fact crucial, otherwise the intrinsically 3D nature of the coordinate system would be inconsistent with the 2D nature of our code, and thus the Einstein equations would not be completely satisfied due to the omission of these contributions. As computational domain, we consider an annulus Ω with inner radius $r_{\min} = 1.8$ and external radius $r_{\max} = 5.0$, discretized by a total number of elements equal to $N_P = 2257$, with characteristic mesh size of $h = \frac{|\Omega|}{N_P} = \frac{\pi(r_{\max}^2 - r_{\min}^2)}{N_P} = 3.0288 \times 10^{-2}$. At both boundaries,

we impose the analytical initial data. Notice also how it is the mesh geometry itself that incorporates the excision zone, which is simply determined by the choice of r_{\min} . Since the coordinates are harmonic in time and space, we use the *harmonic gauge condition* for H_a . Moreover, we set the damping parameters to $\gamma_0 = \gamma_2 = 1, \gamma_1 = -1$. Figure 7 shows the results of this test case obtained using the fourth order version of the ADER-DG schemes, together with a visual representation of the computational domain Ω and the associated unstructured polygonal mesh.

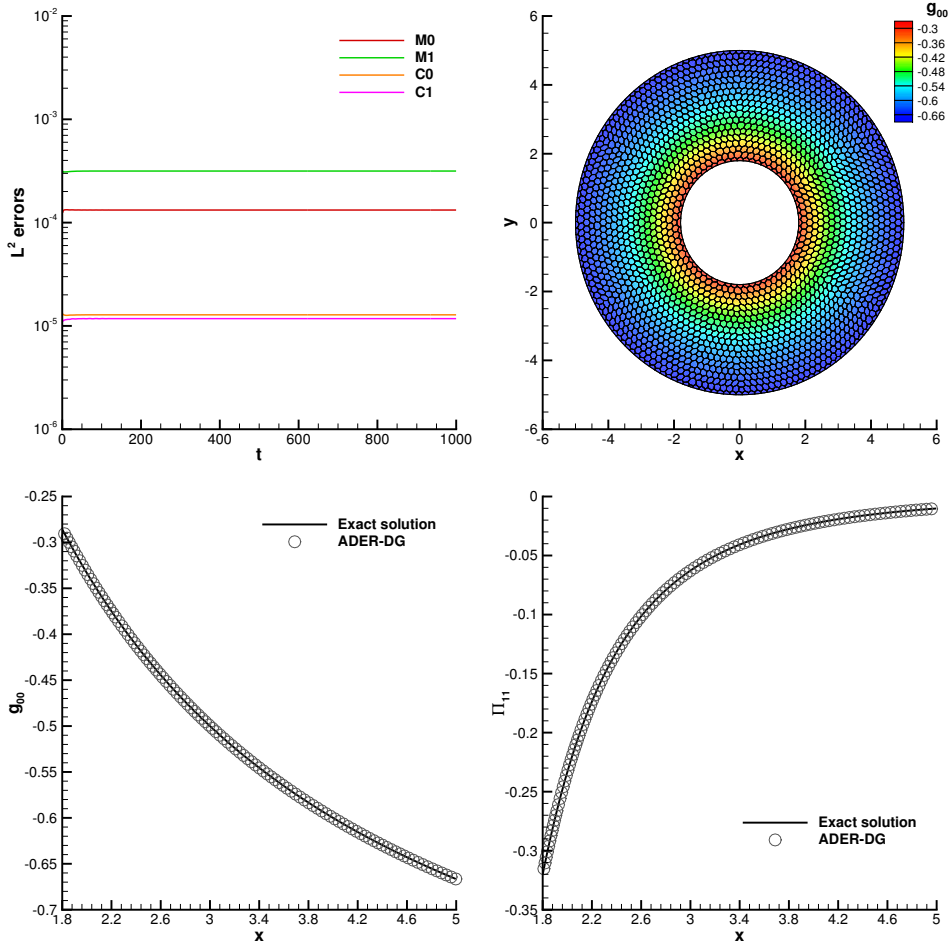


Figure 7: 2D Schwarzschild black hole in 3D Cartesian harmonic coordinates evolved over the equatorial plane $z = 0$ using the fourth order ADER-DG scheme. Top-left panel: time evolution of the constraints. Top-right panel: 2D color contour of g_{00} at final time $t = 1000$, including a detail of the polygonal mesh elements. Bottom panels: comparison of the exact and numerical solution for the variable g_{00} and Π_{11} at final time $t = 1000$ on a one dimensional cut at $y = 0$.

Rotating black hole in 2D. Next, we evolve two Kerr black holes, one with spin $a = 0.5$, and the other one with extreme spin $a = 0.99$, using the same coordinates, setting, and resolution as in the first 2D non-rotating test case described above. We also retain the same structure for the numerical test, that is, we apply a Gaussian perturbation to the variable g_{00} as in Eq. (45). Figure 8 shows the time evolution of the constraints for the two cases, confirming again that the well-balancing feature allows the solutions to come back again to the correct equilibrium states up to machine precision.

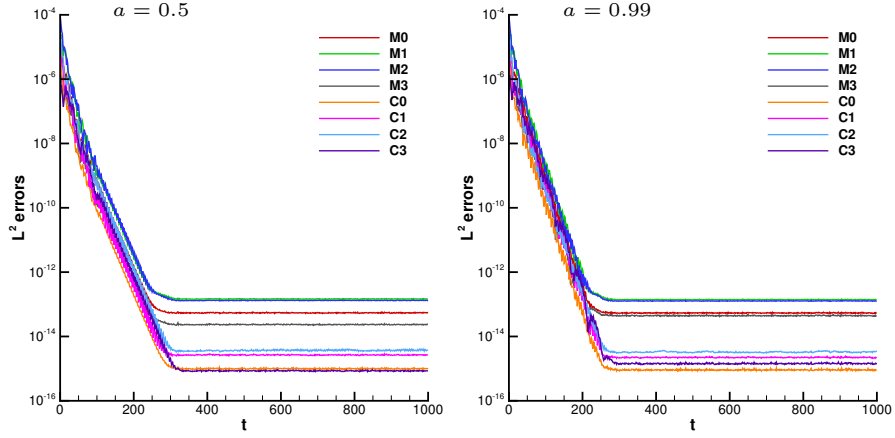


Figure 8: 2D Kerr black holes subject to an initial Gaussian perturbation in the variable g_{00} using the well-balanced fourth order ADER-DG scheme. Time evolution of the constraints for spin $a = 0.5$ on the left, and for extreme spin $a = 0.99$ on the right. In both cases the perturbation decays so that the exact equilibrium state is recovered.

Non-rotating black hole in 3D. We now turn to tests in three space dimensions using the 3D Cartesian Kerr-Schild coordinates [105], first by evolving a stationary Schwarzschild black hole ($a = 0$). Here the computational domain is defined by $\Omega = [-5, 5]^3$, from which we have excised a cubic volume with a half-edge length of unity, centered on the physical singularity at $r = 0$, i.e. $\Omega_e = [-1, 1]^3$. Figure 9 shows the results obtained using the seventh order version of our CWENO-FD schemes with a resolution of 132^3 grid points, and damping parameters set to $\gamma_0 = \gamma_2 = 1$, $\gamma_1 = -1$. Notice that the central panel, which represents a 2D cut on the equatorial plane $z = 0$ with detail of the shift vector field near the singularity, is mainly used as a visual representation, as the cube Ω_e is not evolved, corresponding indeed to the excision region.

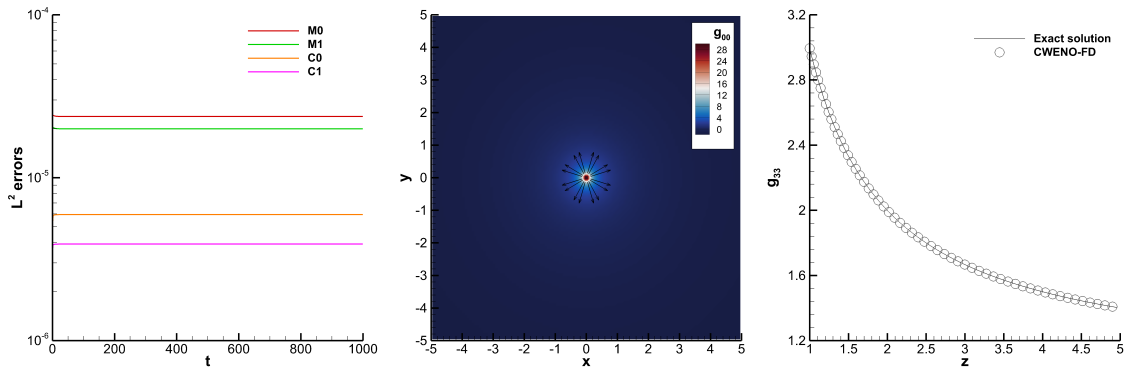


Figure 9: 3D Schwarzschild black hole in Cartesian Kerr-Schild coordinates using the seventh order CWENO-FD scheme. Left panel: time evolution of the constraints. Central panel: 2D cut on the equatorial plane $z = 0$ at final time $t = 1000$ with detail of the shift vector field near the singularity. Right panel: comparison of the exact and numerical solution for the variable g_{33} at final time $t = 1000$ on a one dimensional cut along the z -axis.

Rotating black hole in 3D. To conclude, we consider two Kerr black holes in three space dimensions, with spins $a = 0.5$ and $a = 0.99$. The domain, resolution, damping parameters, and scheme adopted are the same

as in the 3D Schwarzschild case. Notice that, unlike the point singularity in the Schwarzschild metric, the Kerr singularity forms a ring with radius a lying in the $z = 0$ plane, the so called *ring singularity*, which we must enclose within the excision region. To this end, we excise cubic volumes with half-edge lengths of 1 and 1.5 for $a = 0.5$ and $a = 0.99$, respectively, both centered at the origin. In Figure 10 we provide the results associated to the two spins discussed.

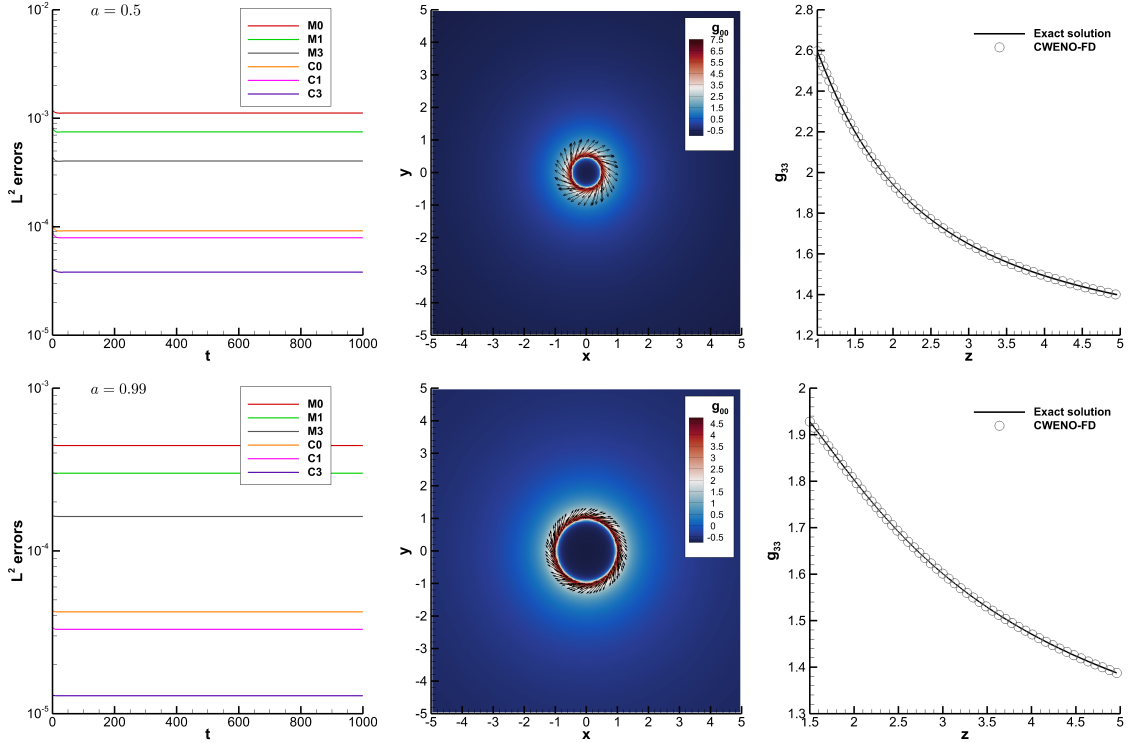


Figure 10: 3D Kerr black hole in Cartesian Kerr-Schild coordinates using the seventh order CWENO-FD scheme. Top panels: spin $a = 0.5$. Bottom panels: spin $a = 0.99$. Left panels: time evolutions of the constraints. Central panels: 2D cuts on the equatorial plane $z = 0$ at final time $t = 1000$ with detail of the shift vector fields near the ring singularities. Right panels: comparisons of the exact and numerical solutions for the variable g_{33} at final time $t = 1000$ on one dimensional cuts along the z -axis.

4.5. Spherical Michel accretion

Accretion can be described as the accumulation of matter onto a compact object due to gravitational attraction, and it constitutes a well-studied problem in astrophysics. The simplest classical model in accretion theory is the spherically symmetric flow of an infinite gas cloud onto a Newtonian point-mass, suggested by Hermann Bondi [22]. A general-relativistic extension was proposed by F. Curtis Michel [82], who considered the spherical accretion of a stationary flow onto a Schwarzschild spacetime (see [91] for a modern presentation of the problem). This represents one of the first studies of spherical accretion onto black holes, and since then, it has inspired several extensions accounting for additional physical effects.

In our work, the fluid is modeled as an ideal gas with adiabatic index $\gamma = 5/3$. The key parameters are the critical radius, where the flow becomes supersonic, which we set to $r_c = 8$, and the critical density, defined as the density at the critical radius, that we choose as $\rho_c = 1/16$ according to [41]. All the details on how to construct the initial condition are presented in [6]. It is essential to emphasize that the Michel solution assumes a static spacetime, and consequently rather than solving the full Einstein-Euler equations,

we evolve only the Euler part while keeping the background metric fixed. This approach, known as the Cowling approximation [37], is justified when the mass accretion rate is small enough that the growth of the black hole mass, potentially originating from the accreted matter, can be safely neglected.

We perform the numerical tests in Kerr-Schild spheroidal coordinates [73] on a computational domain $(r, \theta) \in [1, 10] \times [\delta, \pi - \delta]$, with $\delta = 0.05$. The gauge source function H_a is computed from the initial metric as $H_a = -\Gamma_a$, and we set all the damping parameters to zero. At the boundaries, we impose the Dirichlet initial data.

We show the results obtained using the fifth order CWENO-FD scheme in Figure 11, where in the left panel we demonstrate mesh convergence by plotting the absolute errors for the density ρ at the final time $t = 1000$ for different radial resolutions. Additionally, in Tables 4 and 5 we present a convergence analysis at time $t = 1$ for the CWENO-FD and ADER-DG schemes, respectively.

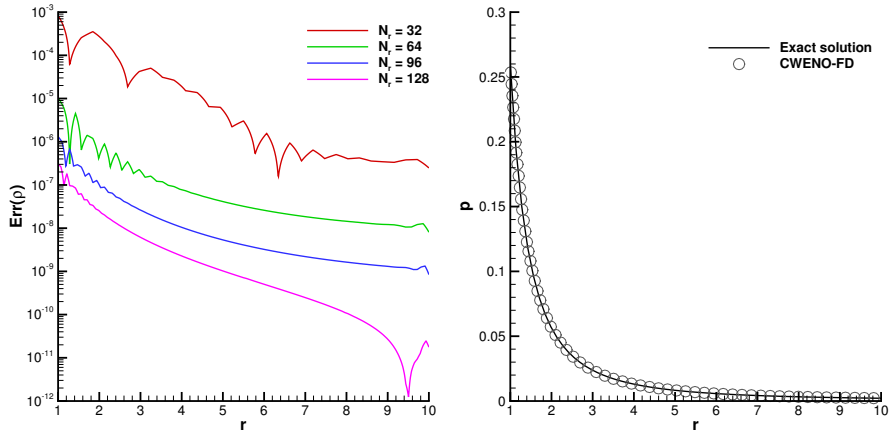


Figure 11: Spherical accretion onto Schwarzschild black hole in 2D spheroidal Kerr-Schild coordinates using the fifth order CWENO-FD scheme. Left panel: absolute errors (computed with respect to the exact solution) for the density ρ at final time $t = 1000$ while increasing the number N_r of radial grid points. Right panel: comparison of the exact and numerical solution for the pressure p at final time $t = 1000$ on a one dimensional cut at $\theta = \pi/2$.

Scheme	$N_r \times N_\theta$	L^2 Error \tilde{D}	$O(\tilde{D})$	Theoretical
CWENO-FD \mathbb{P}_4	128×64	3.1814E-08	-	5.00
	256×128	1.4794E-09	4.43	
	512×256	5.7317E-11	4.69	
CWENO-FD \mathbb{P}_6	128×64	7.8714E-10	-	7.00
	192×96	7.2139E-11	5.89	
	256×128	1.2307E-11	6.15	

Table 4: Numerical convergence results for the spherical accretion onto Schwarzschild black hole in 2D spheroidal Kerr-Schild coordinates at final time $t = 1$ for the conserved variable $\tilde{D} := \sqrt{\gamma}D = \sqrt{\gamma}\rho W$ using the CWENO-FD schemes.

4.6. Non-rotating neutron star in equilibrium

Neutron stars are extremely dense astrophysical objects that result from the gravitational collapse of massive star cores. Even though formulating comprehensive models of their structure is quite complex, there exist some relatively simple standard setups that are commonly used to test the ability of numerical

Scheme	N_x	h	L^2 Error \tilde{D}	$O(\tilde{D})$	Theoretical
ADER-DG \mathbb{P}_1	80	4.2075E-02	6.1397E-03	-	
	120	2.7900E-02	2.6688E-03	2.03	2.00
	160	2.1037E-02	1.5310E-03	1.97	
ADER-DG \mathbb{P}_2	40	8.2836E-02	5.9163E-04	-	
	80	4.2075E-02	8.2674E-05	2.91	3.00
	120	2.7900E-02	2.3864E-05	3.02	
ADER-DG \mathbb{P}_3	40	8.2836E-02	1.4810E-05	-	
	80	4.2075E-02	9.9158E-07	3.99	4.00
	120	2.7900E-02	1.8447E-07	4.09	
ADER-DG \mathbb{P}_4	20	1.6567E-01	4.5139E-06	-	
	40	8.2836E-02	1.9273E-07	4.55	5.00
	80	4.2075E-02	8.9232E-09	4.54	

Table 5: Numerical convergence results for the spherical accretion onto Schwarzschild black hole in 2D spheroidal Kerr-Schild coordinates at final time $t = 1$ for the conserved variable $\tilde{D} := \sqrt{\gamma}D = \sqrt{\gamma}\rho W$ using the ADER-DG schemes.

relativity codes to evolve the full Einstein-Euler system, while also giving a first insight into real astrophysical applications. A representative one is the evolution of an *equilibrium non-rotating neutron star* over long timescales. We therefore consider the Tolman-Oppenheimer-Volkoff (TOV) equations [83, 102]

$$\frac{dm}{dr} = 4\pi r^2(\rho h - p), \quad (46)$$

$$\frac{dp}{dr} = -\frac{\rho h(m + 4\pi r^3 p)}{r(r - 2m)}, \quad (47)$$

$$\frac{d\phi}{dr} = -\frac{1}{\rho h} \frac{dp}{dr}, \quad (48)$$

where $m(r)$ is the mass enclosed within the radius r , ϕ is the unknown metric function in the line element

$$ds^2 = -e^{2\phi} dt^2 + e^{2\psi} dr^2 + r^2 d\Omega^2, \quad (49)$$

while $e^{-2\psi} = 1 - \frac{2m}{r}$. When coupled with an equation of state (EoS), the TOV system completely determines the physical properties of a spherically symmetric body in equilibrium, such as the internal pressure and density profiles, as well as its total mass and radius. Here we consider the polytropic EoS $p = K\rho^\gamma$, and we choose the model parameters according to [58], meaning a central rest mass density $\rho_c = 1.28 \times 10^{-3}$, $K = 100$, and $\gamma = 2$. We then integrate numerically the ODEs (46)–(48) with a tenth order accurate discontinuous Galerkin scheme [44], obtaining a total mass $M = 1.4 M_\odot$ and a radius $R = 9.585 M_\odot = 14.15 \text{ km}$. As described in [30], the standard approach is to introduce the isotropic radius $\bar{r} = \bar{r}(r)$, and to apply the change of coordinates

$$\frac{d\bar{r}}{\bar{r}} = \left(1 - \frac{2m}{r}\right)^{-1/2} \frac{dr}{r}, \quad (50)$$

which makes the spatial part of the metric (49) conformally flat, i.e.

$$ds^2 = -e^{2\phi} dt^2 + e^{2\bar{\psi}}(d\bar{r}^2 + \bar{r}^2 d\Omega^2) = -e^{2\phi} dt^2 + e^{2\bar{\psi}}(d\bar{x}^2 + d\bar{y}^2 + d\bar{z}^2), \quad (51)$$

where $e^{2\bar{\psi}}\bar{r}^2 = r^2$. In the exterior of the star, the spacetime is that of a Schwarzschild solution produced by a mass M , as a consequence of Birkoff's theorem, while all the hydrodynamic variables vanish. We underline that, contrary to what is usually done, we do not impose any artificial atmosphere since we use the filter for the conversion from the conserved to the primitive variables introduced in [54]. To conclude the description of the construction of the solution, we recall that since we need the initial data at arbitrary \bar{r} , interpolation is needed.

For our simulations, we consider a three-dimensional domain $\Omega = [-15, 15]^3$ discretized with 128^3 points, and we use the fifth order version of the CWENO-FD schemes. The gauge source function H_a is computed from the initial data through $H_a = -\Gamma_a$, and we set the damping parameters to $\gamma_0 = 0.1, \gamma_1 = -1, \gamma_2 = 0.5$. We add a small perturbation of amplitude 10^{-4} to the initial pressure p , so that $\tilde{p} = p(1+10^{-4})$, and we compare the results obtained with and without well-balancing. More precisely, in the left panel of Figure 12 we show the time evolution of the normalized central density up to final time $t = 1000$, from which it is evident that the well-balanced approach leads to a much more stable dynamics, while in the right panel of the same figure we further extend the simulation up to $t = 2000$ for the well-balanced case only, in order to highlight its long term robustness. Finally, in Figure 13, we show the time evolution of the constraints.

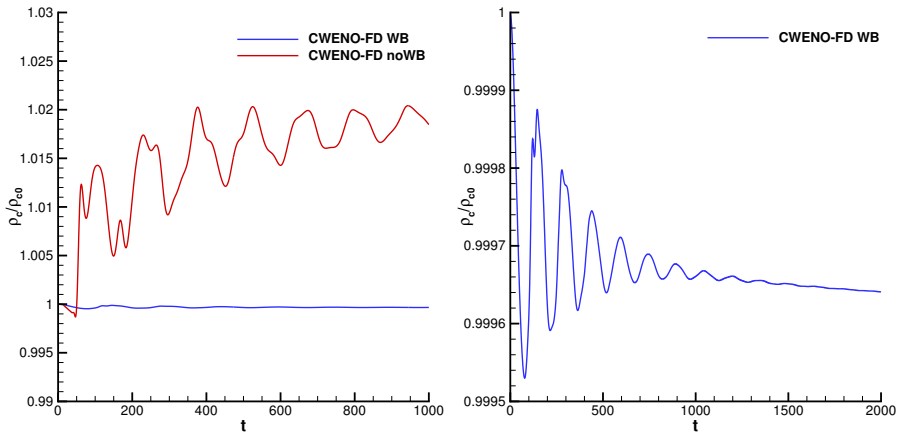


Figure 12: Time evolution of the normalized central density for the perturbed non-rotating neutron star solved with the fifth order CWENO-FD scheme. Left panel: comparison of the well-balanced (WB) and non well-balanced (noWB) versions up to the final time $t = 1000$. Right panel: profile up to the final time $t = 2000$ only in the well-balanced case.

5. Conclusions

In this paper, we have tested two distinct families of high order numerical schemes for nonlinear hyperbolic systems of balance laws applied to the Generalized Harmonic (GH) formulation of the Einstein equations first introduced in [79]: a CWENO-FD scheme on Cartesian grids in two and three space dimensions, and an ADER-DG scheme on unstructured polygonal meshes in two space dimensions. Both approaches were endowed with a well-balancing feature, enabling the exact discrete preservation of known stationary solutions. The successful reproduction of a wide variety of standard vacuum benchmarks confirmed the robustness and accuracy of our schemes when applied to numerical relativity problems. Moreover, the inclusion of matter evolution through the general relativistic Euler equations allowed us to further validate our methods also in a more complete regime, namely coupling the spacetime and matter parts, through tests such as the spherical accretion onto a Schwarzschild black hole and the non-rotating neutron star in

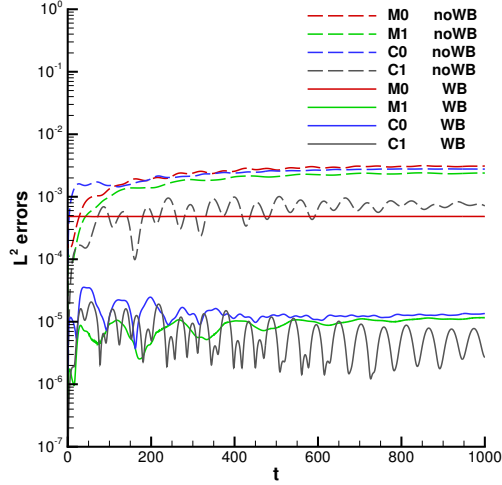


Figure 13: Time evolution of the constraints for the perturbed non-rotating neutron star. Comparison between the well-balanced (WB) and non well-balanced (noWB) fifth order CWENO-FD schemes.

equilibrium. These results establish a solid basis for the next stages of development of this work, for which it is appropriate to offer a few comments. A first natural extension consists in generalizing the ADER-DG scheme to a complete 3D framework on unstructured meshes, ultimately supporting the study of more realistic astrophysical sources beyond axisymmetric systems. Furthermore, the integration of moving meshes within an Arbitrary-Lagrangian-Eulerian (ALE) framework with topology changes [61] represents another key step towards accurate simulations of dynamical spacetimes, such as those encountered in rotating binary systems. We recall that, within the GH formulation, neutron star and black hole mergers have recently been simulated successfully with high order DG schemes in [42] and [81], respectively. The first of these two scenarios, in fact, constitutes the main target we aim to address in our future works, potentially including the extraction of gravitational waves.

6. Acknowledgments

All the authors of this paper are members of the Gruppo Nazionale Calcolo Scientifico-Istituto Nazionale di Alta Matematica (GNCS-INDAM) and would like to acknowledge the CINECA award under the ISCRA initiative, for the availability of high-performance computing resources and support.

M. Dumbser and O. Zanotti acknowledge the support received via the Departments of Excellence Initiative 2018–2027 attributed to DICAM of the University of Trento (grant L. 232/2016). M. Dumbser also acknowledges the funding received via the Fondazione Caritro under the project SOPHOS.

E. Gaburro and S. Muzzolon gratefully acknowledge the support received from the European Union with the ERC Starting Grant *AlcHyMiA* (grant agreement No. 101114995). Views and opinions expressed are however those of the authors only and do not necessarily reflect those of the European Union or the European Research Council. Neither the European Union nor the granting authority can be held responsible for them.

References

[1] M. Alcubierre. *Introduction to 3+1 numerical relativity*, volume 140. Oxford University Press, 2008.

[2] M. Alcubierre, G. Allen, C. Bona, D. Fiske, T. Goodale, F. S. Guzmán, I. Hawke, S. H. Hawley, S. Husa, M. Koppitz, C. Lechner, D. Pollney, D. Rideout, M. Salgado, E. Schnetter, E. Seidel, H. Shinkai, D. Shoemaker, B. Szilágyi, R. Takahashi, and J. Winicour. Towards standard testbeds for numerical relativity. *Classical and Quantum Gravity*, 21(2):589–613, January 2004.

[3] D. Alic, C. Bona-Casas, C. Bona, L. Rezzolla, and C. Palenzuela. Conformal and covariant formulation of the Z4 system with constraint-violation damping. *Physical Review D*, 85(6):064040, 2012.

[4] D. Alic, W. Kastaun, and L. Rezzolla. Constraint damping of the conformal and covariant formulation of the Z4 system in simulations of binary neutron stars. *Physical Review D*, 88(6):064049, 2013.

[5] K. Alvi. First-order symmetrizable hyperbolic formulations of Einstein’s equations including lapse and shift as dynamical fields. *Classical and Quantum Gravity*, 19(20):5153–5162, October 2002.

[6] L. Antón, O. Zanotti, J. A. Miralles, J. M. Martí, J. M. Ibáñez, J. A. Font, and J. A. Pons. Numerical 3+1 general relativistic magnetohydrodynamics: a local characteristic approach. *The Astrophysical Journal*, 637(1):296, 2006.

[7] E. Audusse, F. Bouchut, M. O. Bristeau, R. Klein, and B. Perthame. A fast and stable well-balanced scheme with hydrostatic reconstruction for shallow water flows. *SIAM Journal on Scientific Computing*, 25(6):2050–2065, 2004.

[8] M. C. Babiuc, B. Szilágyi, and J. Winicour. Harmonic initial-boundary evolution in general relativity. *Phys. Rev. D*, 73:064017, Mar 2006.

[9] D. S. Balsara, D. Bhoriya, C.-W. Shu, and H. Kumar. Efficient Finite Difference WENO Scheme for Hyperbolic Systems with Non-Conservative Products. *arXiv e-prints*, page arXiv:2303.17672, March 2023.

[10] D. S. Balsara, D. Bhoriya, C.-W. Shu, and H. Kumar. Efficient Alternative Finite Difference WENO Schemes for Hyperbolic Systems with Non-Conservative Products. *arXiv e-prints*, page arXiv:2403.01266, March 2024.

[11] D. S. Balsara, D. Bhoriya, O. Zanotti, and M. Dumbser. Well-balanced High-order Finite Difference Weighted Essentially Nonoscillatory Schemes for a First-order Z4 Formulation of the Einstein Field Equations. *The Astrophysical Journal Supplement Series*, 275(1):18, November 2024.

[12] D. S. Balsara and M. Dumbser. Divergence-free MHD on unstructured meshes using high order finite volume schemes based on multidimensional Riemann solvers. *Journal of Computational Physics*, pages 687–715, 2015.

[13] D. S. Balsara, M. Dumbser, and R. Abgrall. Multidimensional HLLC Riemann Solver for Unstructured Meshes - With Application to Euler and MHD Flows. *Journal of Computational Physics*, 261:172–208, 2014.

[14] F. Banyuls, J. A. Font, J. M. Ibáñez, J. M. Martí, and J. A. Miralles. Numerical 3+1 general relativistic hydrodynamics: A local characteristic approach. *The Astrophysical Journal*, 476(1):221, 1997.

[15] T. W. Baumgarte and S. L. Shapiro. Numerical integration of Einstein’s field equations. *Physical Review D*, 59(2):024007, 1998.

[16] T. W. Baumgarte and S. L. Shapiro. *Numerical relativity: solving Einstein’s equations on the computer*. Cambridge University Press, 2010.

- [17] J. P. Berberich, P. Chandrashekhar, and C. Klingenberg. High order well-balanced finite volume methods for multi-dimensional systems of hyperbolic balance laws. *Computers and Fluids*, 219:104858, 2021.
- [18] A. Bermudez and M. E. Vázquez-Cendón. Upwind methods for hyperbolic conservation laws with source terms. *Computers & Fluids*, 23(8):1049–1071, 1994.
- [19] C. Birke, W. Boscheri, and C. Klingenberg. A well-balanced semi-implicit IMEX finite volume scheme for ideal magnetohydrodynamics at all Mach numbers. *Journal of Scientific Computing*, 98(2):34, 2024.
- [20] C. Bona, T. Ledvinka, C. Palenzuela, and M. Zácek. Symmetry-breaking mechanism for the Z4 general-covariant evolution system. *Phys. Rev. D*, 69(6):064036, March 2004.
- [21] C. Bona and C. Palenzuela-Luque. *Elements of Numerical Relativity*. Springer-Verlag, Berlin, 2005.
- [22] H. Bondi. On spherically symmetrical accretion. *Monthly Notices of the Royal Astronomical Society*, 112(2):195–204, 1952.
- [23] W. Boscheri and M. Dumbser. Arbitrary–Lagrangian–Eulerian One–Step WENO Finite Volume Schemes on Unstructured Triangular Meshes. *Communications in Computational Physics*, 14:1174–1206, 2013.
- [24] W. Boscheri and M. Dumbser. A direct Arbitrary-Lagrangian-Eulerian ADER-WENO finite volume scheme on unstructured tetrahedral meshes for conservative and non-conservative hyperbolic systems in 3D. *Journal of Computational Physics*, 275:484 – 523, 2014.
- [25] W. Boscheri and M. Dumbser. Arbitrary-Lagrangian-Eulerian discontinuous Galerkin schemes with a posteriori subcell finite volume limiting on moving unstructured meshes. *Journal of Computational Physics*, 346:449 – 479, 2017.
- [26] W. Boscheri, M. Dumbser, and O. Zanotti. High Order Cell-Centered Lagrangian-Type Finite Volume Schemes with Time-Accurate Local Time Stepping on Unstructured Triangular Meshes. *Journal of Computational Physics*, 291:120–150, 2015.
- [27] N Botta, R Klein, S Langenberg, and S Lützenkirchen. Well balanced finite volume methods for nearly hydrostatic flows. *Journal of Computational Physics*, 196(2):539–565, 2004.
- [28] M. Boyle, L. Lindblom, H. P. Pfeiffer, M. A. Scheel, and L. E. Kidder. Testing the accuracy and stability of spectral methods in numerical relativity. *Phys. Rev. D*, 75:024006, Jan 2007.
- [29] J. D. Brown, P. Diener, S. E. Field, J. S. Hesthaven, F. Herrmann, A. H. Mroué, O. Sarbach, E. Schnetter, M. Tiglio, and M. Wagman. Numerical simulations with a first-order BSSN formulation of Einstein’s field equations. *Phys. Rev. D*, 85(8):084004, April 2012.
- [30] M. Bugner. *Discontinuous Galerkin methods for general relativistic hydrodynamics*. PhD thesis, Friedrich-Schiller-Universität Jena, 2018.
- [31] S. Busto, S. Chiocchetti, M. Dumbser, E. Gaburro, and I. Peshkov. High order ADER schemes for continuum mechanics. *Frontiers in Physics*, 8:32, 2020.
- [32] M. J. Castro, J. Gallardo, and C. Parés. High order finite volume schemes based on reconstruction of states for solving hyperbolic systems with nonconservative products. Applications to shallow-water systems. *Mathematics of computation*, 75(255):1103–1134, 2006.

- [33] M. J. Castro, J. M. Gallardo, J. A. López, and C. Parés. Well-balanced high order extensions of Godunov's method for semilinear balance laws. *SIAM Journal on Numerical Analysis*, 46(2):1012–1039, 2008.
- [34] M. J. Castro and C. Parés. Well-balanced high-order finite volume methods for systems of balance laws. *Journal of Scientific Computing*, 82(2):1–48, 2020.
- [35] G. B. Cook and M. A. Scheel. Well-behaved harmonic time slices of a charged, rotating, boosted black hole. *Physical Review D*, 56(8):4775, 1997.
- [36] I. Cordero-Carrión, J. M. Ibáñez, E. Gourgoulhon, J. L. Jaramillo, and J. Novak. Mathematical issues in a fully constrained formulation of the Einstein equations. *Phys. Rev. D*, 77(8):084007, April 2008.
- [37] T. G. Cowling. The non-radial oscillations of polytropic stars. *Mon. Not. R. Astron. Soc.*, 101:367, 1941.
- [38] I. Cravero, G. Puppo, M. Semplice, and G. Visconti. CWENO: uniformly accurate reconstructions for balance laws. *Mathematics of Computation*, 87(312):1689–1719, 2018.
- [39] I. Cravero and M. Semplice. On the accuracy of WENO and CWENO reconstructions of third order on nonuniform meshes. *Journal of Scientific Computing*, 67(3):1219–1246, 2016.
- [40] T. De Donder. The mathematical theory of relativity. 1927.
- [41] L. Del Zanna, O. Zanotti, N. Bucciantini, and P. Londrillo. ECHO: a Eulerian conservative high-order scheme for general relativistic magnetohydrodynamics and magnetodynamics. *Astronomy & Astrophysics*, 473(1):11–30, 2007.
- [42] N. Deppe, F. Foucart, M. S. Bonilla, M. Boyle, N. J. Corso, M. D. Duez, M. Giesler, F. Hébert, L. E. Kidder, Y. Kim, P. Kumar, I. Legred, G. Lovelace, E. R. Most, J. Moxon, K. C. Nelli, H. P. Pfeiffer, M. A. Scheel, S. A. Teukolsky, W. Throwe, and N. L. Vu. Binary neutron star mergers using a discontinuous Galerkin-finite difference hybrid method. *Classical and Quantum Gravity*, 41(24):245002, December 2024.
- [43] N. Deppe, W. Throwe, L. E. Kidder, N. L. Vu, K. C. Nelli, C. Armaza, M. S. Bonilla, F. Hébert, Y. Kim, P. Kumar, G. Lovelace, A. Macedo, J. Moxon, E. O’Shea, H. P. Pfeiffer, M. A. Scheel, S. A. Teukolsky, N. A. Wittek, I. Anantpurkar, C. Anderson, M. Boyle, A. Carpenter, A. Ceja, H. Chaudhary, N. Corso, L. N. Fayyazuddin, F. Foucart, N. Ghadiri, M. Giesler, J. S. Guo, S. Habib, C. Huang, D. A. B. Iozzo, K. Z. Jones, G. Lara, I. Legred, D. Li, S. Ma, D. Melchor, I. Mendes, M. Morales, E. R. Most, M. Murphy, P. J. Nee, A. Osorio, M. A. Pajkos, K. Pannone, V. Prasad, T. Ramirez, N. Ring, H. R. Rüter, J. Sanchez, L. C. Stein, D. Tellez, S. Thomas, V. Tommasini, D. Vieira, T. Włodarczyk, D. Wu, and J. Yoo. SpECTRE, August 2025.
- [44] M. Dumbser. Arbitrary high order PNPM schemes on unstructured meshes for the compressible Navier–Stokes equations. *Computers & Fluids*, 39:60–76, 2010.
- [45] M. Dumbser, D. S. Balsara, E. F. Toro, and C.-D. Munz. A unified framework for the construction of one-step finite volume and discontinuous Galerkin schemes on unstructured meshes. *Journal of Computational Physics*, 227(18):8209–8253, 2008.
- [46] M. Dumbser, W. Boscheri, M. Semplice, and G. Russo. Central weighted ENO schemes for hyperbolic conservation laws on fixed and moving unstructured meshes. *SIAM Journal on Scientific Computing*, 39(6):A2564–A2591, 2017.

[47] M. Dumbser, M. J. Castro, C. Parés, and E. F. Toro. ADER schemes on unstructured meshes for Non-Conservative hyperbolic systems: Applications to geophysical flows. *Computers and Fluids*, 38:1731—1748, 2009.

[48] M. Dumbser, C. Enaux, and E. F. Toro. Finite volume schemes of very high order of accuracy for stiff hyperbolic balance laws. *Journal of Computational Physics*, 227:3971–4001, 2008.

[49] M. Dumbser, F. Fambri, E. Gaburro, and A. Reinarz. On GLM curl cleaning for a first order reduction of the CCZ4 formulation of the Einstein field equations. *Journal of Computational Physics*, 404:109088, 2020.

[50] M. Dumbser, F. Guercilena, S. Köppel, L. Rezzolla, and O. Zanotti. Conformal and covariant Z4 formulation of the Einstein equations: Strongly hyperbolic first-order reduction and solution with discontinuous Galerkin schemes. *Physical Review D*, 97(8):084053, 2018.

[51] M. Dumbser, A. Hidalgo, M. J. Castro, C. Parés, and E. F. Toro. FORCE schemes on unstructured meshes II: Non-conservative hyperbolic systems. *Computer Methods in Applied Mechanics and Engineering*, 199(9):625–647, 2010.

[52] M. Dumbser and C.-D. Munz. Building blocks for arbitrary high order discontinuous Galerkin schemes. *Journal of Scientific Computing*, 27:215–230, 2006.

[53] M. Dumbser and O. Zanotti. Very high order PNPM schemes on unstructured meshes for the resistive relativistic MHD equations. *Journal of Computational Physics*, 228(18):6991–7006, 2009.

[54] M. Dumbser, O. Zanotti, E. Gaburro, and I. Peshkov. A well-balanced discontinuous Galerkin method for the first-order Z4 formulation of the Einstein–Euler system. *J. Comput. Phys.*, 504:112875, 2024.

[55] M. Dumbser, O. Zanotti, and I. Peshkov. High-order discontinuous Galerkin schemes with subcell finite volume limiter and adaptive mesh refinement for a monolithic first-order BSSNOK formulation of the Einstein–Euler equations. *Phys. Rev. D*, 110(8):084015, October 2024.

[56] M. Dumbser, O. Zanotti, and G. Puppo. Monolithic first-order BSSNOK formulation of the Einstein–Euler equations and its solution with path-conservative finite difference central WENO schemes. *Phys. Rev. D*, 111(10):104072, May 2025.

[57] F. Fambri, M. Dumbser, S. Köppel, L. Rezzolla, and O. Zanotti. ADER discontinuous Galerkin schemes for general-relativistic ideal magnetohydrodynamics. *Monthly Notices of the Royal Astronomical Society*, 477(4):4543–4564, 2018.

[58] J. A. Font, T. Goodale, S. Iyer, M. Miller, L. Rezzolla, E. Seidel, N. Stergioulas, W.-M. Suen, and M. Tobias. Three-dimensional numerical general relativistic hydrodynamics. II. Long-term dynamics of single relativistic stars. *Physical Review D*, 65(8):084024, April 2002.

[59] E. Gaburro. A unified framework for the solution of hyperbolic PDE systems using high order direct Arbitrary–Lagrangian–Eulerian schemes on moving unstructured meshes with topology change. *Archives of Computational Methods in Engineering*, 28(3):1249–1321, 2021.

[60] E. Gaburro. High order well-balanced Arbitrary-Lagrangian-Eulerian ADER discontinuous Galerkin schemes on general polygonal moving meshes. *Computers & Fluids*, 301:106764, 2025.

[61] E. Gaburro, W. Boscheri, S. Chiocchetti, C. Klingenberg, V. Springel, and M. Dumbser. High order direct Arbitrary-Lagrangian-Eulerian schemes on moving Voronoi meshes with topology changes. *Journal of Computational Physics*, 407:109167, 2020.

[62] E. Gaburro, M. J. Castro, and M. Dumbser. A Well Balanced Finite Volume Scheme for General Relativity. *SIAM Journal on Scientific Computing*, 43(6):B1226–B1251, January 2021.

[63] E. Gaburro and S. Chiocchetti. High-order Arbitrary-Lagrangian-Eulerian schemes on crazy moving Voronoi meshes. In *Young Researchers Conference*, pages 99–119. Springer, 2021.

[64] E. Gaburro, M. Dumbser, and M. J. Castro. Direct Arbitrary-Lagrangian-Eulerian finite volume schemes on moving nonconforming unstructured meshes. *Computers & Fluids*, 159:254–275, 2017.

[65] G. Gassner, M. Dumbser, F. Hindenlang, and C.-D. Munz. Explicit One-Step time discretizations for discontinuous Galerkin and finite volume schemes based on local predictors. *Journal of Computational Physics*, 230:4232–4247, 2011.

[66] D. Ghosh and E. M. Constantinescu. Well-Balanced, Conservative Finite Difference Algorithm for Atmospheric Flows. *AIAA Journal*, 54(4):1370–1385, 2016.

[67] L. Gosse. A well-balanced scheme using non-conservative products designed for hyperbolic systems of conservation laws with source terms. *Mathematical Models and Methods in Applied Sciences*, 11(02):339–365, 2001.

[68] E. Gourgoulhon. *3+1 Formalism in General Relativity*, volume 846. 2012.

[69] D. Hilditch, S. Bernuzzi, M. Thierfelder, Z. Cao, W. Tichy, and B. Brügmann. Compact binary evolutions with the Z4c formulation. *Phys. Rev. D*, 88:084057, Oct 2013.

[70] G. S. Jiang and C.-W. Shu. Efficient implementation of weighted ENO schemes. *Journal of Computational Physics*, 126:202–228, 1996.

[71] R. P. Kerr. Gravitational field of a spinning mass as an example of algebraically special metrics. *Phys. Rev. Lett.*, 11:237–238, 1963.

[72] L. E. Kidder, S. E. Field, F. Foucart, E. Schnetter, S. A. Teukolsky, A. Bohn, N. Deppe, P. Diener, F. Hébert, J. Lippuner, J. Miller, C. D. Ott, M. A. Scheel, and T. Vincent. SpECTRE: A task-based discontinuous Galerkin code for relativistic astrophysics. *Journal of Computational Physics*, 335:84–114, April 2017.

[73] S. S. Komissarov. Electrodynamics of black hole magnetospheres. *Monthly Notices of the Royal Astronomical Society*, 350(2):427–448, 2004.

[74] R. J. LeVeque. Balancing source terms and flux gradients in high-resolution Godunov methods: the quasi-steady wave-propagation algorithm. *Journal of Computational Physics*, 146(1):346–365, 1998.

[75] D. Levy, G. Puppo, and G. Russo. Central WENO schemes for hyperbolic systems of conservation laws. *Mathematical Modelling and Numerical Analysis*, 33(3):547 – 571, 1999.

[76] D. Levy, G. Puppo, and G. Russo. Third order central WENO scheme for 2D conservation laws. *Applied Numerical Mathematics*, 33(1):415 – 421, 2000.

[77] D. Levy, G. Puppo, and G. Russo. Compact central WENO schemes for multidimensional conservation laws. *SIAM Journal on Scientific Computing*, 22(2):656 – 672, 2001.

[78] L. Lindblom, K. D. Matthews, O. Rinne, and M. A. Scheel. Gauge drivers for the generalized harmonic Einstein equations. *Physical Review D—Particles, Fields, Gravitation, and Cosmology*, 77(8):084001, 2008.

[79] L. Lindblom, M. A. Scheel, L. E. Kidder, R. Owen, and O. Rinne. A new generalized harmonic evolution system. *Classical and Quantum Gravity*, 23(16):S447–S462, August 2006.

[80] L. Lindblom and B. Szilágyi. Improved gauge driver for the generalized harmonic Einstein system. *Phys. Rev. D*, 80:084019, Oct 2009.

[81] G. Lovelace, K. C. Nelli, N. Deppe, N. L. Vu, W. Throwe, M. S. Bonilla, A. Carpenter, L. E. Kidder, A. Macedo, M. A. Scheel, A. Afram, M. Boyle, A. Ceja, M. Giesler, S. Habib, K. Z. Jones, P. Kumar, G. Lara, D. Melchor, I. B. Mendes, K. Mitman, M. Morales, J. Moxon, E. O’Shea, K. Pannone, H. P. Pfeiffer, T. Ramirez-Aguilar, J. Sanchez, D. Tellez, S. A. Teukolsky, and N. A. Wittek. Simulating binary black hole mergers using discontinuous Galerkin methods. *Classical and Quantum Gravity*, 42(3):035001, 2025.

[82] F. C. Michel. Accretion of matter by condensed objects. *Astrophysics and Space Science*, 15(1):153–160, 1972.

[83] J. R. Oppenheimer and G. M. Volkoff. On massive neutron cores. *Physical Review*, 55(4):374, 1939.

[84] C. Parés. Numerical methods for nonconservative hyperbolic systems: a theoretical framework. *SIAM Journal on Numerical Analysis*, 44(1):300–321, 2006.

[85] L. Pareschi and T. Rey. Residual equilibrium schemes for time dependent partial differential equations. *Computers & Fluids*, 156:329–342, 2017.

[86] B. Perthame and C. Simeoni. A kinetic scheme for the Saint-Venant system with a source term. *Calcolo*, 38(4):201–231, 2001.

[87] F. Pretorius. Evolution of Binary Black-Hole Spacetimes. *Phys. Rev. Letters*, 95(12):121101, September 2005.

[88] F. Pretorius. Numerical relativity using a generalized harmonic decomposition. *Classical and Quantum Gravity*, 22(2):425–451, January 2005.

[89] J. Qiu, M. Dumbser, and C.-W. Shu. The discontinuous Galerkin method with Lax-Wendroff type time discretizations. *Computer Methods in Applied Mechanics and Engineering*, 194:4528–4543, 2005.

[90] T. C. Rebollo, A. D. Domínguez, and E. D. N. Fernández. A family of stable numerical solvers for the shallow water equations with source terms. *Computer methods in applied mechanics and engineering*, 192(1-2):203–225, 2003.

[91] L. Rezzolla and O. Zanotti. *Relativistic hydrodynamics*. Oxford University Press, 2013.

[92] K. Schwarzschild. Über das Gravitationsfeld eines Massenpunktes nach der Einsteinschen Theorie. *Sitzungsberichte der Königlich Preussischen Akademie der Wissenschaften*, pages 189–196, January 1916.

[93] M. Semplice, A. Coco, and G. Russo. Adaptive mesh refinement for hyperbolic systems based on third-order compact WENO reconstruction. *Journal of Scientific Computing*, 66(2):692–724, 2016.

[94] M. Shibata and T. Nakamura. Evolution of three-dimensional gravitational waves: Harmonic slicing case. *Physical Review D*, 52(10):5428, 1995.

[95] C.-W. Shu and S. Osher. Efficient implementation of essentially non-oscillatory shock capturing schemes. *Journal of Computational Physics*, 77:439–471, 1988.

[96] C.-W. Shu and S. Osher. Efficient implementation of essentially non-oscillatory shock capturing schemes II. *Journal of Computational Physics*, 83:32–78, 1989.

[97] V. Springel. E pur si muove: Galilean-invariant cosmological hydrodynamical simulations on a moving mesh. *Monthly Notices of the Royal Astronomical Society*, 401(2):791–851, 2010.

[98] H. Tang, T. Tang, and K. Xu. A gas-kinetic scheme for shallow-water equations with source terms. *Zeitschrift für angewandte Mathematik und Physik ZAMP*, 55(3):365–382, 2004.

[99] A. Thomann, G. Puppo, and C. Klingenberg. An all speed second order well-balanced IMEX relaxation scheme for the Euler equations with gravity. *Journal of Computational Physics*, 4201:109723, 2020.

[100] W. Tichy, A. Adhikari, and L. Ji. Evolving neutron stars with the Nmesh code. In *APS April Meeting Abstracts*, volume 2021 of *APS Meeting Abstracts*, page S08.003, January 2021.

[101] W. Tichy, L. Ji, A. Adhikari, A. Rashti, and M. Pirog. The new discontinuous Galerkin methods based numerical relativity program Nmesh. *Classical and Quantum Gravity*, 40(2):025004, January 2023.

[102] R. C. Tolman. Static solutions of Einstein’s field equations for spheres of fluid. *Physical Review*, 55(4):364, 1939.

[103] E. F. Toro, R. C. Millington, and L. A. M. Nejad. Towards very high order Godunov schemes. In *Godunov methods: theory and applications*, pages 907–940. Springer, 2001.

[104] P. Tsoutsanis, E. M. Adebayo, A. C. Merino, A. P. Arjona, and M. Skote. CWENO finite-volume interface capturing schemes for multicomponent flows using unstructured meshes. *Journal of Scientific Computing*, 89(3):64, 2021.

[105] M. Visser. The Kerr spacetime: A brief introduction. *arXiv e-prints*, page arXiv:0706.0622, June 2007.

[106] O. Zanotti and M. Dumbser. A high order special relativistic hydrodynamic and magnetohydrodynamic code with space-time adaptive mesh refinement. *Computer Physics Communications*, 188:110–127, 2015.

[107] O. Zanotti, F. Fambri, and M. Dumbser. Solving the relativistic magnetohydrodynamics equations with ADER discontinuous Galerkin methods, a posteriori subcell limiting and adaptive mesh refinement. *Mon. Not. R. Astron. Soc.*, 452:3010–3029, September 2015.